Analysis of vehicle path tracking ability and lateral stability on a floating bridge under a crosswind

Journal of Wind Engineering & Industrial Aerodynamics 227 (2022) 105070

Contents lists available at ScienceDirect

Journal of Wind Engineering & Industrial Aerodynamics

journal homepage: www.elsevier.com/locate/jweia

Analysis of vehicle path tracking ability and lateral stability on a floating bridge under a crosswind

Dragan Sekulic [a,*,1], Alexey Vdovin [a], Bengt Jacobson [a], Simone Sebben [a], Stian Moe Johannesen [b]

[a] Chalmers University of Technology, Gothenburg, Sweden
[b] The Norwegian Public Road Administration, Oslo, Norway

ARTICLE INFO

Keywords:
Floating bridge
Wind loads
Lateral stability
Tracking ability
Vehicle safety
Tractor-semitrailer
SUV
Vehicle modelling

ABSTRACT

The reconstructed route E39 along the west coast of Norway will provide efficient local and regional transportation for people and goods. Efficient transportation implies safety measures exist, e.g., driving speed limits for adverse weather condition. This is especially important for structures in open areas, such as long-span bridges. This paper investigates the path tracking ability and lateral stability of two vehicle types – a tractor-semitrailer (TS) and a sport utility vehicle (SUV) – on the Bjørnafjorden floating bridge considering a 1-year storm condition. At a speed of 108 km/h, the TS experiences a roll-over risk, and at a speed of 90 km/h, it frequently leaves the traffic lane. At the highest speed, the SUV wheels do not lose contact with the bridge deck, but the vehicle does leave the traffic lane. This implies that a TS driver requires more vehicle handling effort over the floating bridge than an SUV driver. Results suggest that a TS can safely enter the bridge at a low speed (36 km/h) and then accelerate to 72 km/h after travelling 2 km. An SUV entering at a speed of 90 km/h and accelerating to 108 km/h after travelling 0.5 km was found to be safe.

1. Introduction

Coastal highway route E39, the largest transportation project in Norway, will provide considerable benefits for society regionally and nationally, such as more efficient transport, improvement of road standards and traffic safety. The new E39 route will reduce the travel time from the southern to the northern part of the country (from Kristiansand to Trondheim) by 11 h. Different types of structures, such as floating bridges, suspension bridges, submerged floating tunnels, and subsea road tunnels, will replace existing ferries on the route. A reduction in travel time will improve the conditions for freight transport and lower driving costs (e.g., fuel/oil consumption, vehicle repairs and maintenance). In addition, other expenses, such as driver/assistant wages, vehicle administration and garaging, will also be reduced (Vegvesen, 2017, 2021). The new road will also improve the conditions for passenger transport, e.g., the time cost for leisure trips and home-to-work trips will be lower.

Efficient transportation of people/goods on the route implies the existence of safety measures suitable for hazardous driving conditions. This is especially important for structures exposed to severe wind and waves during inclement weather, such as long-span bridges. In the past, safety measures on bridges under windy conditions were usually established on subjective experiences (Chen and Cai, 2004), without conclusions from proper numerical investigations.

Ride comfort and driving safety for two vehicle types (light truck and sedan car) running on the coastal slender cable-stayed bridge subjected to wind and wave loads were investigating in (Zhu, J. et al., 2018). Analysis was done numerically using 13 degrees of freedom (DOFs) vehicle models. Investigation indicated that the effects of wave on the overall vibration total values, the roll safety criteria and the sideslip safety criteria were much less than those from the wind. Driving safety and comfort for high-sided vehicle (truck of 11 DOFs) in a slender arch bridge under turbulent wind were investigated in (Nguyen, K. et al., 2017). The results showed that bridge vibration was significantly affected by the crosswind in terms of peak acceleration and frequency content. The crosswind had more effect on the ride comfort of the

* Corresponding author.
E-mail addresses: dragan.sekulic@chalmers.se (D. Sekulic), alexey.vdovin@chalmers.se (A. Vdovin), bengt.jacobson@chalmers.se (B. Jacobson), simone.sebben@chalmers.se (S. Sebben), stian.moe.johannesen@vegvesen.no (S.M. Johannesen).
[1] d.sekulic@sf.bg.ac.rs

https://doi.org/10.1016/j.jweia.2022.105070
Received 9 November 2021; Received in revised form 17 June 2022; Accepted 17 June 2022
Available online 25 June 2022

vehicle in the lateral direction and on its safety in terms of overturning accidents. Safety analysis of high-sided road vehicle (large truck of 19 DOFs) running on a long span cable-stayed bridge under a sharp-edged crosswind gust while the bridge was oscillating under fluctuating winds had been investigating in (Guo and Xu, 2006). Analysis showed that the oscillation of the cable-stayed bridge would lower the accident vehicle speed when wind speed reached a certain level.

Floating bridges have been considered a crossing solution over the Bjørnafjorden floating bridge (Fig. 1). The effects of floating bridge vertical motion on a bus driver's ride comfort and road grip were analysed (Sekulic, D. 2018; Sekulic et al., 2020a,b) for different speeds based on numerical simulations and a driving simulator. The influence of vertical vibration was found to be mainly relevant at low frequency, i.e., motion sickness. The contact between the wheel and floating bridge deck was assessed by the dynamic load coefficient. The values were found to be within the range of the values for heavy vehicle exploitation on stationary roads in good condition. The results from driving simulator tests for a bus and a passenger car confirmed greater difficulty in staying within the traffic lane under bridge motion and aerodynamic loads, unlike driving on a (non)-moving road without aerodynamic loads (Gustafsson et al., 2019). The lateral stability of an intercity bus model under floating bridge motion excitations and wind has been recently investigated (Sekulic, 2018). Simulation results revealed that the vehicle deviation from the path increases with increasing bus speed. Roll-over risk was confirmed at a bus speed of 108 km/h since the windward rear wheels lost contact with the moving bridge deck.

The influence of floating bridge motion together with aerodynamic loads on the lateral stability of multiunit heavy vehicles and SUVs is an area that has not been investigated enough. The lateral dynamics behaviour of multi-unit heavy vehicles becomes complex since the aerodynamic loads must be considered separately to account for the articulation angle effects.

The first aim of this paper is to define vehicle dynamics models suitable for the investigation of *bridge-vehicle-driver-wind* interactions using two vehicle types, a tractor-semitrailer (TS) and a sport utility vehicle (SUV). The second aim is to analyse vehicle path tracking ability, vehicle stability and driver load for a 1-year storm driving condition over a floating bridge. Based on the results, the study suggests appropriate vehicle speeds for safe crossing over the Bjørnafjorden floating bridge. MATLAB/Simulink software was used for vehicle modelling and numerical simulation.

2. Vehicle models

When defining the TS model, a Lagrangian method was used. This method is convenient when modelling complex vehicle systems with more units. Unlike Newton's method, a Lagrangian formulation does not introduce reaction forces at the coupling point (fifth wheel), and the number of equation terms is correspondingly fewer. In the case of the SUV model, Newton's second law and D'Alembert's principle were used for the definition of the differential equations of motion (EOMs).

2.1. Tractor semitrailer model definition

For vehicle path-tracking ability and stability investigation, a three-rigid-axle TS model with 9 degrees of freedom (DOFs) was defined. The in-road-plane DOFs are the longitudinal motion, lateral motion, yaw motion of the tractor (X, Y, ψ_1) and articulation angle (Θ) (Fig. 2). The out-of-road-plane DOFs include the roll motions of the tractor unsprung mass, semitrailer unsprung mass, tractor front and rear axles, and semitrailer axle (φ_1, φ_2, φ_{fa}, φ_{ra}, and φ_{sa}) (Fig. 3). The notations in Fig. 3 and the vehicle parameters and their values are provided in the Appendix (Table 1, Table 3). These values were obtained from the available literature (Jacobson, 2020; Yang et al., 2015; MSC. Software, 2013; Sekulic et al., 2013; Lin et al., 1996; Jeyed and Ali Ghaffari, 2019) and are typical for this type of vehicle.

It was considered that the suspension system at the tractor front axle contains two air springs (an air spring on the left side – k_{sfl}; an air spring on the right side – k_{sfr}), four shock absorbers (two shock absorbers on the left side – $c_{dfl} = 2\ c_{d,fa}$; two shock absorbers on the right side – $c_{dfr} = 2\ c_{d,fa}$) and an anti-roll bar ($k_{arb,fa}$). Air spring stiffness (k_{sfl}, k_{sfr}) values, single shock-absorber damping ($c_{d,fa}$) value, equivalent shock-absorber damping (c_{dfl}, c_{dfr}) values and an anti-roll bar torsional stiffness ($k_{arb,fa}$) value are presented in the Appendix (Table 1). The suspension system at the tractor rear axle includes four air springs (two air springs on the left side – $k_{srl} = 2{\cdot}k_{s,ra}$; two air springs on the right side – $k_{srr} = 2{\cdot}k_{s,ra}$), four shock absorbers (two shock absorbers on the left side – $c_{drl} = 2\ c_{d,ra}$; two shock absorbers on the right side – $c_{drr} = 2\ c_{d,ra}$) and an anti-roll bar ($k_{arb,ra}$). Single air spring stiffness ($k_{s,ra}$) value, equivalent air spring stiffness (k_{srl}, k_{srr}) values, single shock-absorber damping ($c_{d,ra}$) value, equivalent shock-absorber damping (c_{drl}, c_{drr}) values and an anti-roll bar torsional stiffness ($k_{arb,ra}$) value are presented in the Appendix (Table 1). The suspension system at the semitrailer axles contains four air springs (two air springs on the left side – $k_{sl} = 2{\cdot}k_{s,sa}$; two air springs on the right side – $k_{sr} = 2{\cdot}k_{s,sa}$), four shock absorbers (two shock absorbers on the left side – $c_{dl} = 2\ c_{d,sa}$; two shock absorbers on the right side – $c_{dr} = 2\ c_{d,sa}$) and an anti-roll bar ($k_{arb,sa}$). Single air spring stiffness ($k_{s,sa}$) value, equivalent air spring stiffness (k_{sl}, k_{sr}) values, single shock-absorber damping ($c_{d,sa}$) value, equivalent shock-absorber damping (c_{dl}, c_{dr}) values and an anti-roll bar torsional stiffness ($k_{arb,sa}$) value are presented in the Appendix (Table 1).

The tractor has two steering wheels on the front axle and two dual-wheels on the rear axle (Fig. 13). The semitrailer has three rigid axles with two dual-wheels on each axle (Fig. 13). These suspension system elements and wheel configurations are standard for a TS (Jacobson, 2020). Radial damping for heavy vehicle tires is small (Nguyen and Le,

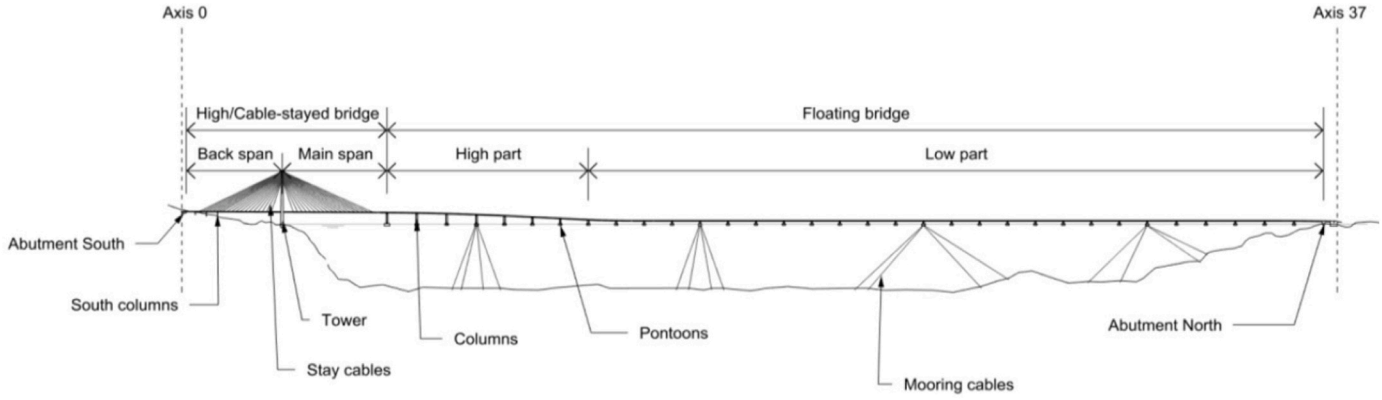

Fig. 1. Bjørnafjorden floating bridge (straight concept solution).

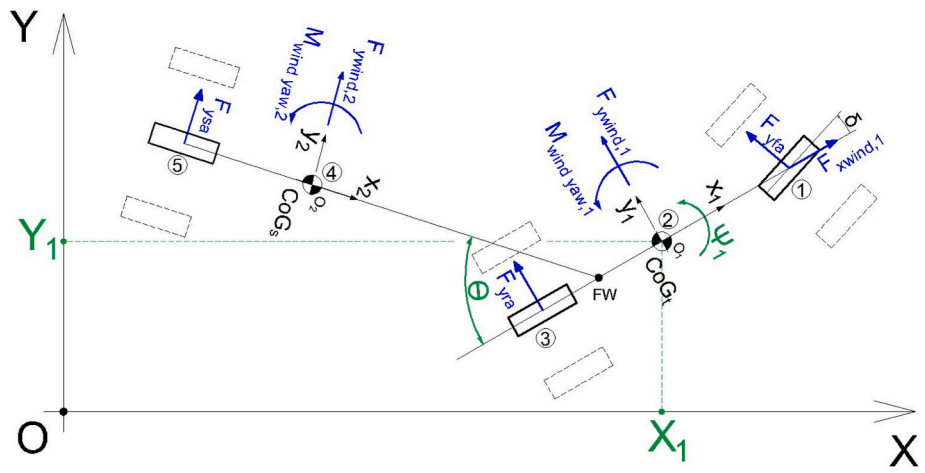

Fig. 2. Vehicle in-plane motion, view from above.

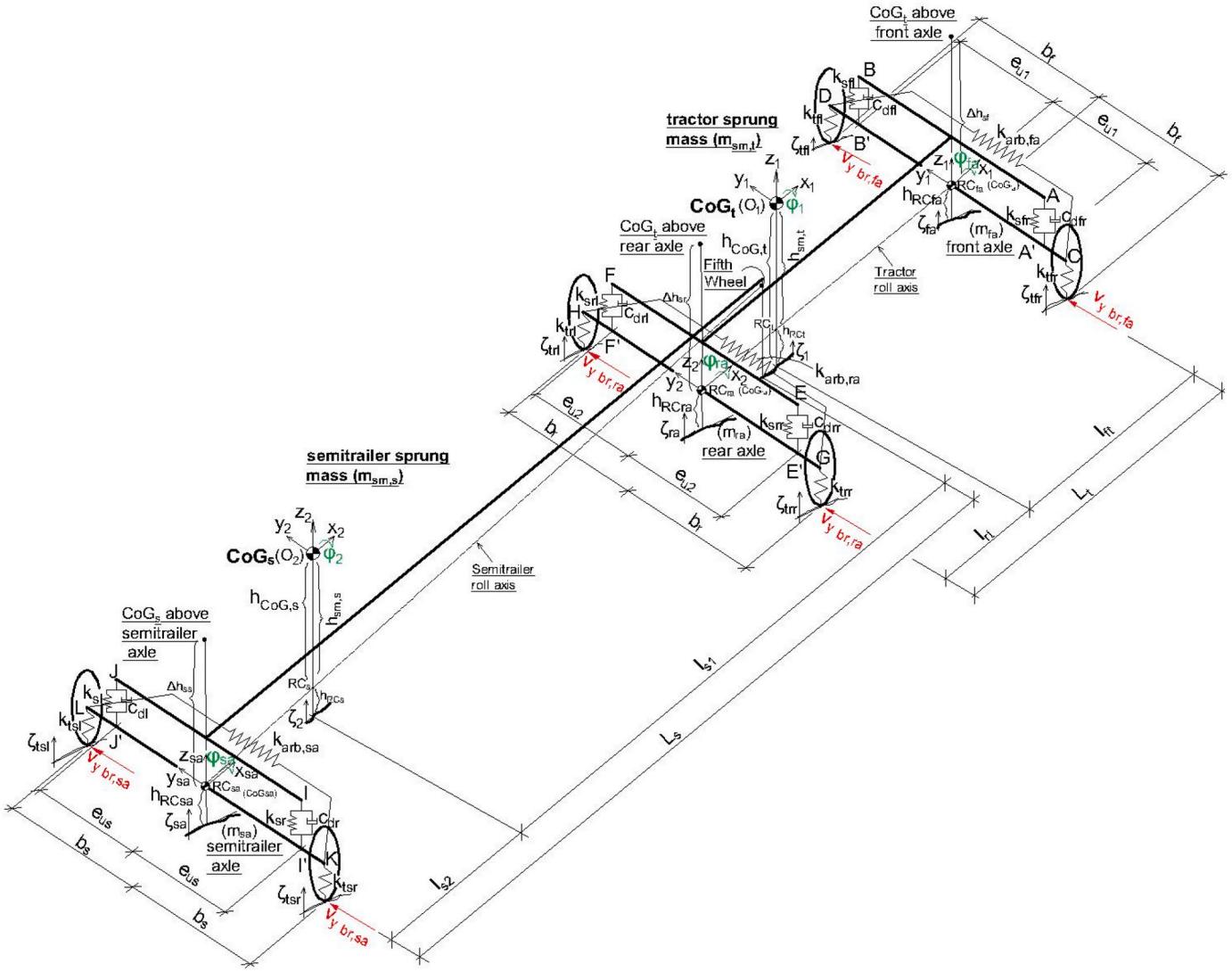

Fig. 3. Vehicle out-of-plane motion and vehicle parameters.

2019; Liu et al., 2001; Gillespie, 1992) and not considered. In the analysis, a TS without loads is considered, as this configuration would have the lowest mass and hence be maximally sensitive to wind loads.

The following limitations and assumptions have been considered:

- The vehicle moves at a constant forward speed (traction and braking compensate for driving resistance);
- The pitch motion of the tractor/semitrailer units is not considered since the vertical bridge displacement has very long wavelengths (Sekulic, 2018);
- The vertical motion of the tractor/semitrailer units is not considered because of the low excitation frequencies from the bridge deck (Sekulic et al., 2020a,b);
- The tractor/semitrailer units are symmetrical relative to their centres of gravity (CoGs) along the longitudinal axis (*x*-axis);
- All springs and damper elements have linear characteristics;
- The tractor/semitrailer bodies and axles are rigid;
- One equivalent axle is considered for the semitrailer unit (this unit has three axles, as shown in Fig. 13);
- Axles can roll with respect to the sprung body to which they are attached;
- The CoG of the tractor/semitrailer sprung mass coincides with the CoG of the whole tractor/semitrailer units since the mass of the tractor/semitrailer body is considerably higher than the masses of their axles;
- The effect of vehicle motion on the bridge is considered nonsignificant since the mass of the floating bridge is much higher than the mass of the considered vehicle (Sekulic, 2018; Siringoringo and Fujino, 2012);
- Roll centres (RCs) for the axles coincide with their CoGs;
- Wind drag force acts only on the tractor unit in the local x_1-direction ($F_{xwind,1}$);
- The articulation joint (TS fifth wheel) has no friction in yaw and is free of a roll moment;

2.1.1. Lagrangian equations for the system

When formulating nonlinear differential equations of motions, a Lagrangian formulation was used (Eq. (1)).

$$\frac{d}{dt}\frac{\partial T}{\partial \dot{q}_i}-\frac{\partial T}{\partial q_i}+\frac{\partial V}{\partial q_i}+\frac{\partial D}{\partial q_i}=Q_i,\ i=1,\ldots,n; \tag{1}$$

where T is the kinetic energy of the system; V is the potential energy of the system; D is the dissipative energy of the system; q_i are generalized coordinates; $\dot{q}_i$ are generalized velocities; Q_i are generalized forces; and n is the total number of generalized coordinates.

The number of generalized coordinates of the system is equal to the number of aforementioned DOFs, and these are

$$q=\left[X_1;\ Y_1;\ \psi_1;\ \theta;\ \varphi_1;\ \varphi_2;\ \varphi_{fa};\ \varphi_{ra};\ \varphi_{sa}\right] \tag{2}$$

In vehicle dynamics, variables and equations are often expressed in the fixed (local) coordinate system of the vehicle. Some reasons for this are the large values of the vehicle yaw angle (Pacejka, 2012), easier derivation of the tire forces (Ghandriz et al., 2020), etc. When considering the local coordinate system of the first unit (tractor), modified equations with new generalized variables (longitudinal velocity, lateral velocity and yaw rate of the tractor (u, v, ω_1; Fig. 4)) should be considered. The form of modified the Lagrangian equations can be found in (Pacejka, 2012). For the generalized coordinates (Θ, φ_1, φ_2, φ_{fa}, φ_{ra}, φ_{sa}), the classical Lagrangian formulation remains, Eq. (1).

2.1.2. Determination of the energies for the system

2.1.2.1. Kinetic energy. The kinetic energy of the system contains the kinetic energies of the rigid bodies due to in-plane and out-of-plane motion. Before determination of the kinetic energy, the longitudinal/lateral velocities of the vehicle rigid bodies CoGs need to be defined (Points 1–7, Fig. 4). Velocities are expressed as a function of appropriate generalized velocities and vehicle geometric parameters and given in their final forms by Eqs. 3–11

- Point 1, (CoG of the tractor front axle),

$$\begin{aligned} u1&=u\\ v1&=v+l_{fi}\omega_1 \end{aligned} \tag{3}$$

- Point 2, (CoG of the tractor unit),

$$\begin{aligned} u2&=u\\ v2&=v \end{aligned} \tag{4}$$

- Point 3, (CoG of the tractor rear axle),

$$\begin{aligned} u3&=u\\ v3&=v-l_{ri}\omega_1 \end{aligned} \tag{5}$$

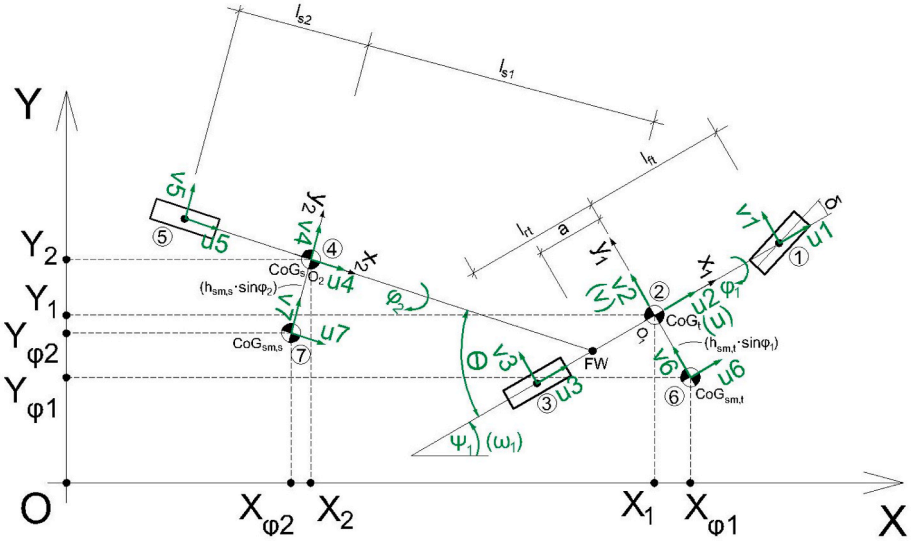

Fig. 4. The velocities of the vehicle rigid body CoGs.

- Point 4, (CoG of the semitrailer unit),

$$u4 = (u + l_{s1}(\dot{\theta} - \omega_1)sin\theta)cos\theta - (v - a\omega_1 + l_{s1}(\dot{\theta} - \omega_1)cos\theta)sin\theta$$
$$v4 = (u + l_{s1}(\dot{\theta} - \omega_1)sin\theta)sin\theta + (v - a\omega_1 + l_{s1}(\dot{\theta} - \omega_1)cos\theta)cos\theta \quad (6)$$

- Point 5, (CoG of the semitrailer axle),

$$u5 = u4$$
$$v5 = v4 - (\omega_1 - \dot{\theta})l_{s2} \quad (7)$$

- Point 6, (CoG of the tractor sprung mass),

$$u6 = u + h_{sm,t}\omega_1 sin\varphi_1$$
$$v6 = v - h_{sm,t}\dot{\varphi}_1 cos\varphi_1 \quad (8)$$

- Point 7, (CoG of the semitrailer sprung mass),

$$u7 = u7' cos\theta - v7' sin\theta$$
$$v7 = u7' sin\theta + v7' cos\theta \quad (9)$$

$$u7' = u4' - h_{sm,s}\dot{\varphi}_2 cos\varphi_2 sin\theta - h_{sm,s}sin\varphi_2 cos\theta(\dot{\theta} - \omega_1)$$
$$v7 = v4' - h_{sm,s}\dot{\varphi}_2 cos\varphi_2 cos\theta + h_{sm,s}sin\varphi_2 sin\theta(\dot{\theta} - \omega_1) \quad (10)$$

$$u4' = u + l_{s1}(\dot{\theta} - \omega_1)sin\theta$$
$$v4' = v - a\omega_1 + l_{s1}(\dot{\theta} - \omega_1)cos\theta \quad (11)$$

After defining the velocities, the kinetic energy could be determined, such as

$$T = T_{in-plane} + T_{out-of-plane} \quad (12)$$

$$T = \frac{1}{2}J_t\dot{\psi}_1^2 + \frac{1}{2}J_s(\dot{\theta} - \omega_1)^2 + \frac{1}{2}m_{fa}(u1^2 + v1^2) + \frac{1}{2}m_{ra}(u3^2 + v3^2) + \frac{1}{2}m_{sa}(u5^2 + v5^2) + \frac{1}{2}m_{sm,t}(u6^2 + v6^2) + \frac{1}{2}m_{sm,s}(u7^2 + v7^2) + \frac{1}{2}J_{fa}\dot{\varphi}_{fa}^2 + \frac{1}{2}J_{ra}\dot{\varphi}_{ra}^2 + \frac{1}{2}J_{sa}\dot{\varphi}_{sa}^2 + \frac{1}{2}J_{sm,t}\dot{\varphi}_1^2 + \frac{1}{2}J_{sm,s}\dot{\varphi}_2^2 \quad (13)$$

2.1.2.2. Potential energy. The potential energy of the system comes from spring deformation (air springs in the suspension system and tires), anti-roll bar deformation and height changes of the sprung mass CoGs due to roll motion.

Considering Fig. 5, the potential energy takes the form shown in Eqs. 14 and 15

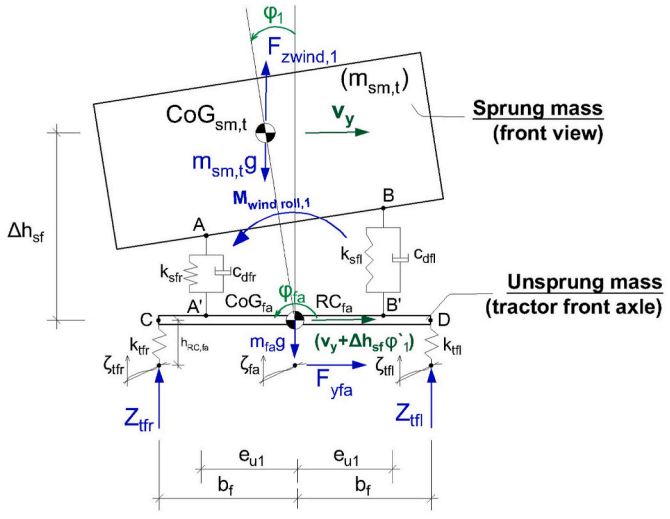

Fig. 5. Roll-dynamics of the tractor.

$$V = \frac{1}{2}k_{sfl}(z_B - z_{B'})^2 + \frac{1}{2}k_{sfr}(z_A - z_{A'})^2 + \frac{1}{2}k_{tfl}(z_D - \zeta_{tfl})^2 + \frac{1}{2}k_{tfr}(z_C - \zeta_{tfr})^2 + \frac{1}{2}k_{srl}(z_F - z_{F'})^2 + \frac{1}{2}k_{srr}(z_E - z_{E'})^2 + \frac{1}{2}k_{trl}(z_H - \zeta_{trl})^2 + \frac{1}{2}k_{trr}(z_G - \zeta_{trr})^2 + \frac{1}{2}k_{sl}(z_J - z_{J'})^2 + \frac{1}{2}k_{sr}(z_I - z_{I'})^2 + \frac{1}{2}k_{tsl}(z_L - \zeta_{tsl})^2 + \frac{1}{2}k_{tsr}(z_K - \zeta_{tsr})^2 + V_{arb(fa;ra;sa)} + V_{\Delta h_{sm(ts)}} \quad (14)$$

$$V = \frac{1}{2}k_{sfl}2e_{u1}^2(\varphi_1 - \varphi_{fa})^2 + \frac{1}{2}k_{srl}2e_{u2}^2(\varphi_1 - \varphi_{ra})^2 + \frac{1}{2}k_{sl}2e_{us}^2(\varphi_2 - \varphi_{sa})^2 + \frac{1}{2}k_{tfl}\left((\zeta_{fa} + b_f\varphi_{fa} - \zeta_{tfl})^2 + (\zeta_{fa} - b_f\varphi_{fa} - \zeta_{tfr})^2\right) + \frac{1}{2}k_{trl}((\zeta_{ra} + b_r\varphi_{ra} - \zeta_{trl})^2 + (\zeta_{ra} - b_r\varphi_{ra} - \zeta_{trr})^2) + \frac{1}{2}k_{tsl}((\zeta_{sa} + b_s\varphi_{sa} - \zeta_{tsl})^2 + (\zeta_{sa} - b_s\varphi_{sa} - \zeta_{tsr})^2) + \frac{1}{2}k_{arb,fa}(\varphi_1 - \varphi_{fa})^2 + \frac{1}{2}k_{arb,ra}(\varphi_1 - \varphi_{ra})^2 + \frac{1}{2}k_{arb,sa}(\varphi_2 - \varphi_{sa})^2 - \frac{1}{2}m_{sm,t}gh_{sm,t}\varphi_1^2 - \frac{1}{2}m_{sm,s}gh_{sm,s}\varphi_2^2 \quad (15)$$

2.1.2.3. Dissipative energy. The dissipative energy of the system originates from dampers in the suspension system. Considering Fig. 5, this energy takes the form shown in Eqs. 16 and 17

$$D = \frac{1}{2}c_{dfl}(\dot{z}_B - \dot{z}_{B'})^2 + \frac{1}{2}c_{dfr}(\dot{z}_A - \dot{z}_{A'})^2 + \frac{1}{2}c_{drl}(\dot{z}_F - \dot{z}_{F'})^2 + \frac{1}{2}c_{drr}(\dot{z}_E - \dot{z}_{E'})^2 + \frac{1}{2}c_{dl}(\dot{z}_J - \dot{z}_{J'})^2 + \frac{1}{2}c_{dr}(\dot{z}_I - \dot{z}_{I'})^2 \quad (16)$$

$$D = \frac{1}{2}c_{dfl}2e_{u1}^2(\dot{\varphi}_1 - \dot{\varphi}_{fa})^2 + \frac{1}{2}c_{drl}2e_{u2}^2(\dot{\varphi}_1 - \dot{\varphi}_{ra})^2 + \frac{1}{2}c_{dl}2e_{us}^2(\dot{\varphi}_2 - \dot{\varphi}_{sa})^2 \quad (17)$$

2.1.2.4. Definition of generalized forces. Generalized forces are given by Eq. (18)

$$Q_i = \sum_{j=1}^{k}\left(\frac{\partial\dot{r}_j}{\partial\dot{q}_i}\right)\cdot F_j;\ i = 1, \ldots, 9;\ \dot{q} = [u;\ v;\ \dot{\psi}_1;\ \dot{\theta};\ \dot{\varphi}_1;\ \dot{\varphi}_2;\ \dot{\varphi}_{fa};\ \dot{\varphi}_{ra};\ \dot{\varphi}_{sa}] \quad (18)$$

where Q_i are generalized forces; $\dot{r}_j$ are velocity vectors (given by Eqs. 3–11) of the points where external forces act (Figs. 2 and 5); F_j are external tire and wind forces (Figs. 2 and 5). In addition to the wind forces, within the aerodynamic loads, wind moments act on the vehicle. External forces imply the wind moment components, whereas velocities imply appropriate angular rates when calculating generalized forces using Eq. (18). MATLAB code was written for the derivation of the Lagrangian equations. Simulink blocks (one block for each generalized coordinate) were used as the outputs from the code and used for the TS model definition.

2.2. SUV model definition

For the SUV, a vehicle dynamics model with 8 DOFs was defined. The in-road-plane DOFs are the lateral motion and yaw motion *(y, ψ1)* (Fig. 6a). The out-of-road-plane DOFs include the roll motion of the vehicle sprung mass, vertical motion of the vehicle body (sprung mass) and each wheel (unsprung masses) *(φxs, z, zflw, zfrw, zfrw and zrrw)* (Fig. 6b). The notations in Fig. 6 and the vehicle parameters and their values are presented in the Appendix (Table 2, Table 3). These values were obtained from the available literature (Jacobson, 2020; Brandt et al., 2021; Shyrokau et al., 2013; Zhang et al., 2019) and are typical values for this type of vehicle. The SUV is equipped with an independent

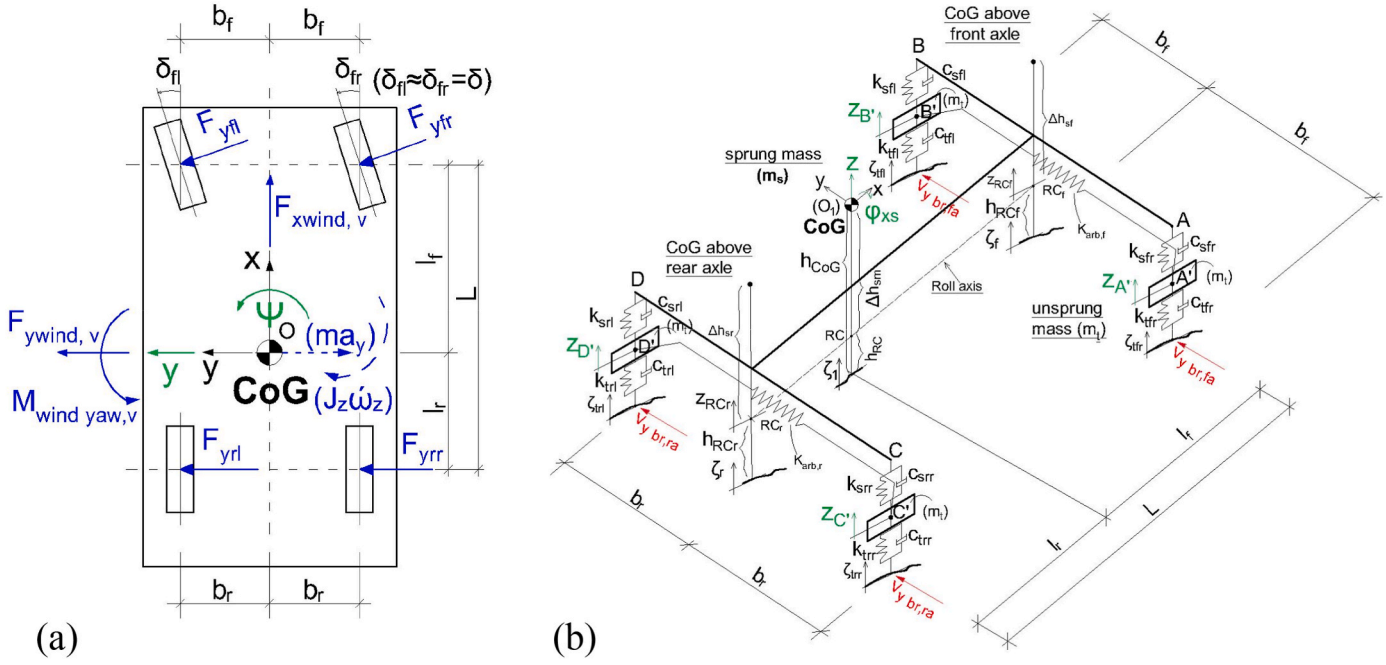

Fig. 6. SUV a) in-plane motion, view from above; b) out-of-plane motion.

suspension system and includes one spring and one shock absorber at each wheel. The suspension system also contains an anti-roll bar at the vehicle front and rear part.

When forming EOMs, all assumptions for the bus model (Sekulic, 2018) applied to the SUV, except those for rigid axles. The SUV has an independent suspension system, and unsprung masses (wheels) are considered point masses (Fig. 6b).

2.2.1. In-road plane motion

The lateral equilibrium for the vehicle is defined by Eq. (19), and the vehicle yaw equilibrium around the z-axis (Fig. 6a) is given by Eq. (20). These equations are the same form as Eqs. (1) and (2) presented in (Sekulic, 2018). The notations in the equations can be found in Table 3 in the Appendix.

$$m\left(\dot{v}_y + v_x\omega_z\right) = F_{yfl}cos\delta + F_{yfr}cos\delta + F_{yrl} + F_{yrr} + F_{ywind,v} \tag{19}$$

$$J_z\dot{\omega_z} = \left(F_{yfl} - F_{yfr}\right)sin\delta b_f + \left(F_{yfl} + F_{yfr}\right)cos\delta l_f - \left(F_{yrl} + F_{yrr}\right)l_r + M_{wind\ yaw,v} \tag{20}$$

2.2.2. Out-of-road plane motion

Free-body diagrams (FBDs) for the SUV sprung mass and unsprung masses are presented in Fig. 7. Active and fictive forces in the vertical direction are also presented in Fig. 7.

The vertical motion of the vehicle sprung mass is given by (Eq. (21)). Here, we presented the equation in its final form, and the procedure of its derivation can be found in (Sekulic, 2018).

$$\begin{aligned} m_s\ddot{z} = &-\left(c_{sfr} + c_{sfl} + c_{srr} + c_{srl}\right)\dot{z} - \left(k_{sfr} + k_{sfl} + k_{srr} + k_{srl}\right)z + c_{sfr}\dot{z}_{A'} + k_{sfr}z_{A'} \\ &+ c_{sfl}\dot{z}_{B'} + k_{sfl}z_{B'} + c_{srr}\dot{z}_{C'} + k_{srr}z_{C'} + c_{srl}\dot{z}_{D'} + k_{srl}z_{D'} + F_{zwind,v} \end{aligned} \tag{21}$$

Unlike the rigid axle with the roll-motion DOF used in the bus model (Sekulic, 2018), the SUV has an independent suspension system.

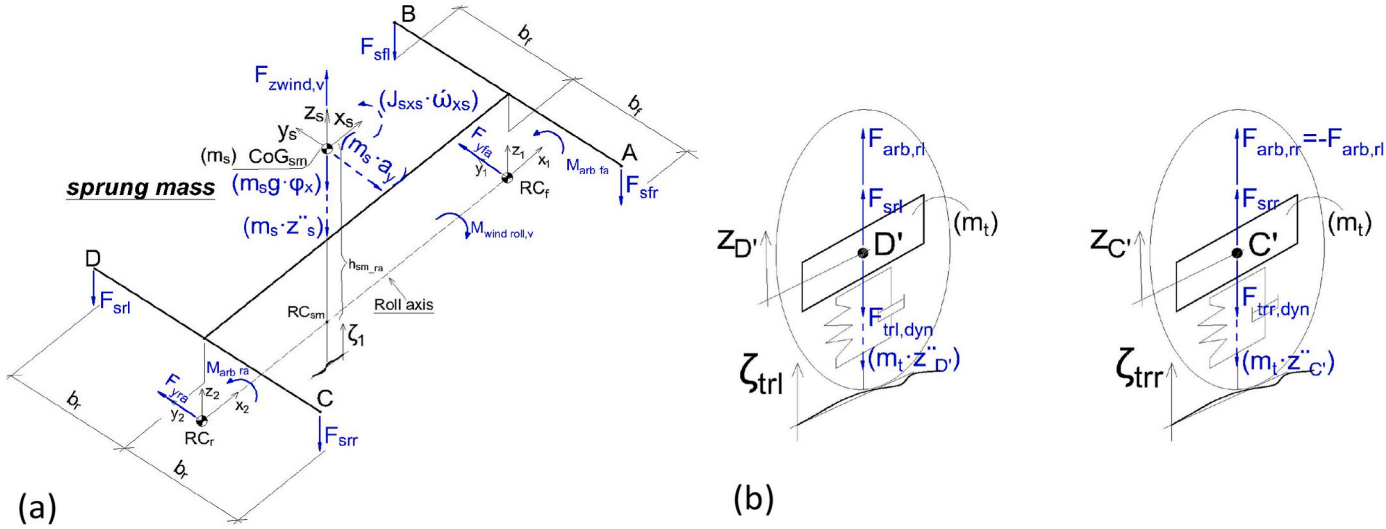

Fig. 7. FBDs of the vertical motion of a) the vehicle body; b) the rear left and right wheel.

Considering the FBD (Fig. 7b), EOMs for the front left/right wheels in their final forms are presented by Eqs. 22 and 23. The EOMs for the rear left/right wheels take the same form as for the front wheels but with different notions.

$$m_t\ddot{z}_{B'} = -\left(c_{sfl}+c_{tfl}\right)\dot{z}_{B'} - \left(k_{sfl}+k_{tfl}\right)z_{B'} + c_{sfl}\dot{z} + k_{sfl}z + c_{sfl}b_f\dot{\varphi}_{xs} + k_{sfl}b_f\varphi_{xs} + c_{tfl}\dot{\zeta}_{fl} + k_{tfl}\zeta_{fl} + k_{arb,f}\frac{1}{2b_f}\left(\varphi_{xs} - \frac{z_{B'}-z_{A'}}{2b_f}\right) \tag{22}$$

$$m_t\ddot{z}_{A'} = -\left(c_{sfr}+c_{tfr}\right)\dot{z}_{A'} - \left(k_{sfr}+k_{tfr}\right)z_{A'} + c_{sfr}\dot{z} + k_{sfr}z - c_{sfr}b_f\dot{\varphi}_{xs} - k_{sfr}b_f\varphi_{xs} + c_{tfr}\dot{\zeta}_{fr} + k_{tfr}\zeta_{fr} - k_{arb,f}\frac{1}{2b_f}\left(\varphi_{xs} - \frac{z_{B'}-z_{A'}}{2b_f}\right) \tag{23}$$

The EOM for the sprung mass roll DOF is given by Eq. (24). The derivation of this equation can be found in (Sekulic, 2018) and is given here in its final form.

$$J_{xx}\dot{\omega_{xs}} = \left(m_s g - F_{z\ wind,v}\right)\Delta h_{sm}\varphi_{xs} + m_s a_y \Delta h_{sm} - \left(\left(2b_f\varphi_{xs} + z_{A'} - z_{B'}\right)k_{sfr} + \left(2b_f\dot{\varphi}_{xs} + \dot{z}_{A'} - \dot{z}_{B'}\right)c_{sfr}\right)2b_f - \left(\left(2b_r\varphi_{xs} + z_{C'} - z_{D'}\right)k_{srr} + \left(2b_r\dot{\varphi}_{xs} + \dot{z}_{C'} - \dot{z}_{D'}\right)c_{srr}\right)2b_r - k_{arb,f}\left(\varphi_{xs} - \frac{z_{B'}-z_{A'}}{2b_f}\right) - k_{arb,r}\left(\varphi_{xs} - \frac{z_{D'}-z_{C'}}{2b_r}\right) + M_{wind\ roll,v} \tag{24}$$

2.3. Tire forces

Brush tire model was used for the tire lateral force calculations in both vehicle models. The brush tire model depends on a few values, given by Eq. (25)

$$F_{y,w} = \begin{cases} -sign\left(s_y\right)\cdot\left(C_y\cdot|s_y| - \frac{\left(C_y\cdot|s_y|\right)^2}{3\cdot Z_w\cdot\mu} + \frac{\left(C_y\cdot|s_y|\right)^3}{27\cdot\left(Z_w\cdot\mu\right)^2}\right); & if \quad |s_y| < \frac{3\cdot Z_w\cdot\mu}{C_y} \\ -sign\left(s_y\right)\cdot\mu\cdot Z_w; & else \end{cases} \tag{25}$$

where $F_{y,w}$ is the lateral tire force on each wheel; C_y is the cornering stiffness; Z_w is the vertical tire force on each wheel; s_y is the lateral tire slip for each wheel; and μ is the road friction coefficient (Table 3).

Cornering stiffness is given by Eq. (26)

$$C_y = C_{cy}\cdot Z_w \tag{26}$$

where C_{cy} is the cornering stiffness coefficient; The corresponding stiffness coefficient C_{cy} takes different values for passenger car and heavy vehicle tires. For a passenger car tire, this value is higher than that for a heavy vehicle tire (Table 3). When calculating vertical tire forces, the same procedure was used as in (Sekulic, 2018).

The lateral tire slip for the wheels on the tractor front axle is given by Eq. (27)

$$s_{tf,y} = \frac{\Delta v_{tf,y}}{u1} = \frac{v1 - v_{y\ br,fa}}{u1} - \delta \tag{27}$$

Similarly, the lateral tire slip for the wheels on the tractor rear axle is given by Eq. (28)

$$s_{tr,y} = \frac{\Delta v_{tr,y}}{u3} = \frac{v3 - v_{y\ br,ra}}{u3} \tag{28}$$

The lateral tire slip for the wheels on the semitrailer axle is given by Eq. (29)

$$s_{s,y} = \frac{\Delta v_{s,y}}{u5} = \frac{v5 - v_{y\ br,sa}}{u5} \tag{29}$$

where $\Delta v_{tf,y}$, $\Delta v_{tr,y}$ and $\Delta v_{s,y}$ are respectively the relative lateral velocities between the tractor front tyres, tractor rear tyres, semitrailer tyres and bridge deck at the contact point; *v1, v3* and *v5* are respectively lateral velocities of the CoG of tractor front axle, tractor rear axle and semitrailer axle; *u1, u3* and *u5* are respectively longitudinal velocities of the CoG of tractor front axle, tractor rear axle and semitrailer axle; $v_{y\ br,fa}$, $v_{y\ br,ra}$ and $v_{y\ br,sa}$ are respectively the lateral velocities of the bridge deck at the tyre contact point for the tractor front axle, tractor rear axle and semitrailer axle; and δ is the steering angle (same for the two front wheels). When calculating lateral tire slip for SUV model, the same procedure was used as for the TS model.

For tire slip calculations, the lateral velocities of the bridge deck at the tire contact point were taken. Fig. 8 shows the bridge deck lateral velocities for the TS tire model inputs for a vehicle speed of 72 km/h. These signals differ slightly due to wheelbase distances and lateral motion of the bridge deck. For a vehicle speed of 72 km/h, the values of the lateral bridge velocity lie within ±0.2 m/s.

Fig. 9b shows the power spectral density (PSD) of the lateral bridge velocities for the tractor front axle as a function of different vehicle speeds. Velocity intensities are mainly concentrated into two frequency ranges, from 0 to 0.1 Hz and 0.2–0.3 Hz. These characteristics are found to be similar for the bridge velocity signals for the tractor second axle and for the semitrailer axle. The presentation of these signals in the frequency domain is of importance in regard to the analysis of the handwheel steer angle (HSA) signals (section 6.2).

2.4. Aerodynamic loads

The aerodynamic coefficients for the TS were determined using Computational Fluid Dynamics (CFD) simulations. The simulation method used was verified experimentally at Chalmers model scale wind tunnel (Dineff, 2021). Several 3D printed generic tractor-trailer combinations were used to compare aerodynamic coefficients obtained in the tunnel and in the corresponding CFD simulations. The magnitudes of forces and trends with changing air angle of attack, especially in the main region of interest (0–45 deg) correlated well. An example of such a comparison for the side force coefficient is shown in Fig. 10.

Fig. 11a–d shows the aerodynamic force/moment coefficients as a function of wind yaw angle for the tractor and semitrailer units. Fig. 11e–f presents the aerodynamic force/moment coefficients as a function of wind yaw angle for the SUV. For the semitrailer and the SUV, Fig. 11c–d, a sudden decline in the lift coefficient is observed at around 40° wind yaw angle. At around this angle and above, the flow is no longer attached to the roof and creates a large, separated area, see Fig. 12 for the case of the semitrailer. This results in increased pressure on the roof and, consequently, decreased lift. This behaviour was also observed experimentally by (Dineff, 2021).

The CFD simulations were performed using steady-state RANS approach, hence, only the averaged flow conditions were considered for each wind yaw angle investigated. Given a transient side wind signal and vehicle velocity, the instantaneous wind yaw and relative vehicle velocity could be calculated. This transient data was used to obtain the signal for magnitudes of aerodynamic forces and moments, imitating realistic flow conditions in presence of wind gusts, see Fig. 16 for an example. Although the bridge deck should have an influence on the aerodynamic loads, particularly the side force, it was not considered in the CFD simulations. This simplification was made to facilitate the computation of multiple configurations at different yaw angles. Additionally, according to Wang and Hariharan (2021), it is expected that with the absence of the deck and wind barriers, the side forces on the vehicle will be larger, representing then a worst scenario input to the vehicle dynamics model as the wind will not be deflected by bridge structures which would provide partial shielding for the vehicle.

The drag force coefficients for the semitrailer unit are lower than those for the tractor unit (Fig. 11a, c). The drag force coefficients for the semitrailer are close to zero since the semitrailer is completely shielded by the tractor unit (Fig. 13).

Fig. 13 shows the TS model used in the CFD simulations with two ISO

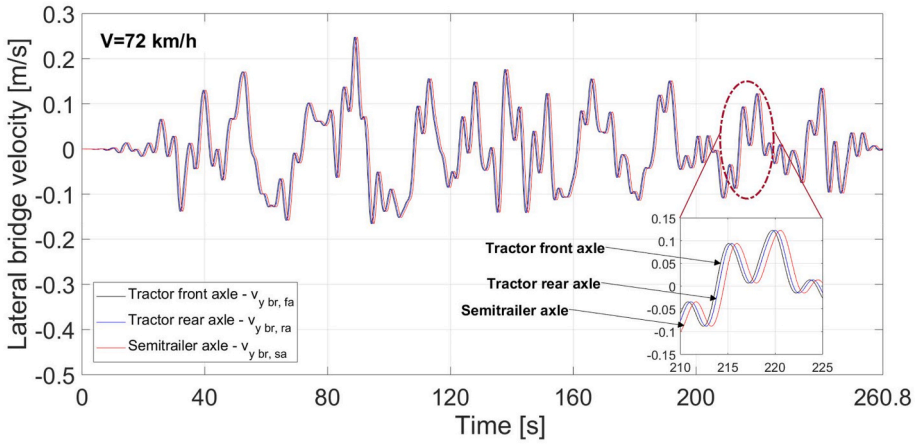

Fig. 8. Bridge lateral velocity for the tire model inputs for the TS axles as a function of time (vehicle speed of 72 km/h).

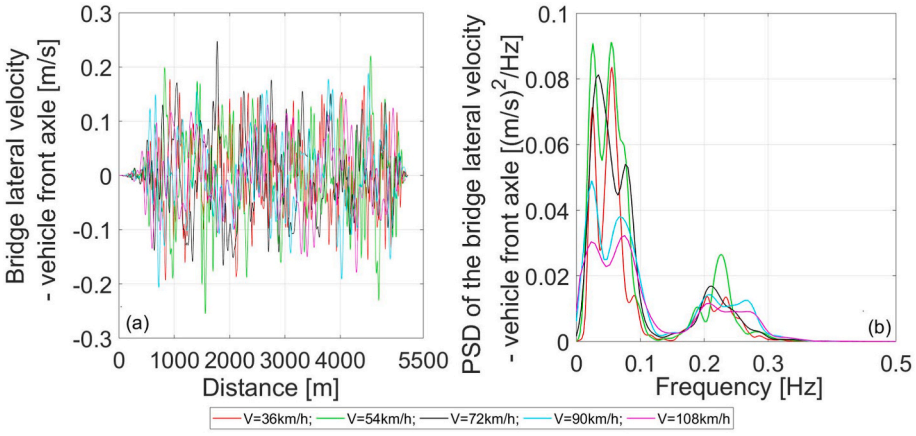

Fig. 9. Bridge lateral velocity for the vehicle front axle as a function of a) distance; b) frequency.

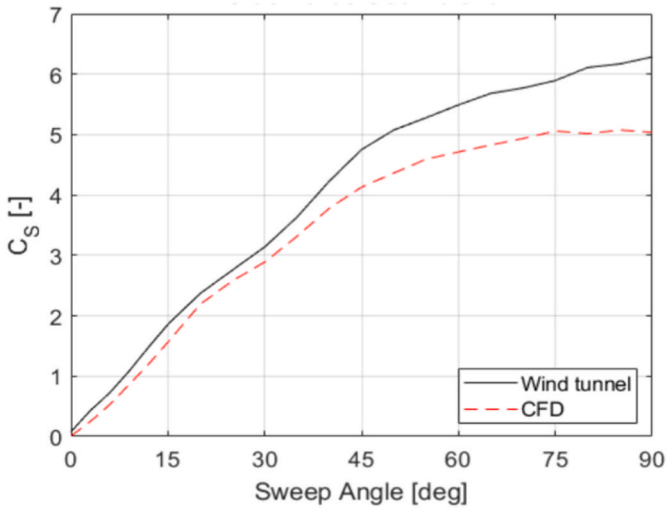

Fig. 10. Comparison between wind tunnel and CFD results for the aerodynamic side force coefficient obtained for simplified truck model.

4130 coordinate systems attached to two reference points (O_t, O_s). The reference point for the tractor unit (O_t) was set up in the ground plane at the position where the line of the tractor front axle projection on the ground intersects the mid-track line of the unit. Similarly, the reference point for the semitrailer unit (O_s) was set up in the ground plane at the position where the line of the semitrailer first axle projection on the ground intersects the mid-track line of the semitrailer unit. A sign convention of the aerodynamic coefficients for both units is denoted, where the arrows indicate positive directions. An ISO 8855 coordinate system was attached to each CoG unit. The RCs are also shown in the figure.

Fig. 14 shows the SUV model used in the CFD simulations. The coordinate system (ISO 4130) is attached to reference point O and was set up in the ground plane at the mid-wheelbase and mid-track positions. The vehicle coordinate system ($O_3x_3y_3z_3$) attached to its CoG is also presented in the figure.

Aerodynamic forces and moments acting on the tractor/semitrailer unit and SUV were calculated using Eqs. 30–35:

$$F_{xwind,i} = sign\left(V_{rel\ wind,i}\right)\cdot\frac{1}{2}\rho V_{rel\ i}^2\cdot A_i\cdot c_{D,i}(\beta_{wi}) \tag{30}$$

$$F_{ywind,i} = sign\left(V_{rel\ wind,i}\right)\cdot\frac{1}{2}\rho V_{rel\ i}^2\cdot A_i\cdot c_{S,i}(\beta_{wi}) \tag{31}$$

$$F_{zwind,i} = \frac{1}{2}\rho V_{rel\ i}^2\cdot A_i\cdot c_{L,i}(\beta_{wi}) \tag{32}$$

$$M_{wind\ roll,i} = (-1)\cdot\frac{1}{2}\rho V_{rel\ i}^2\cdot A_i\cdot L_i\cdot\left(c_{R,i}(\beta_{wi}) + \frac{h_{CoG,i} - h_{RC,i}}{L_i}\cdot c_{S,i}(\beta_{wi})\right) \tag{33}$$

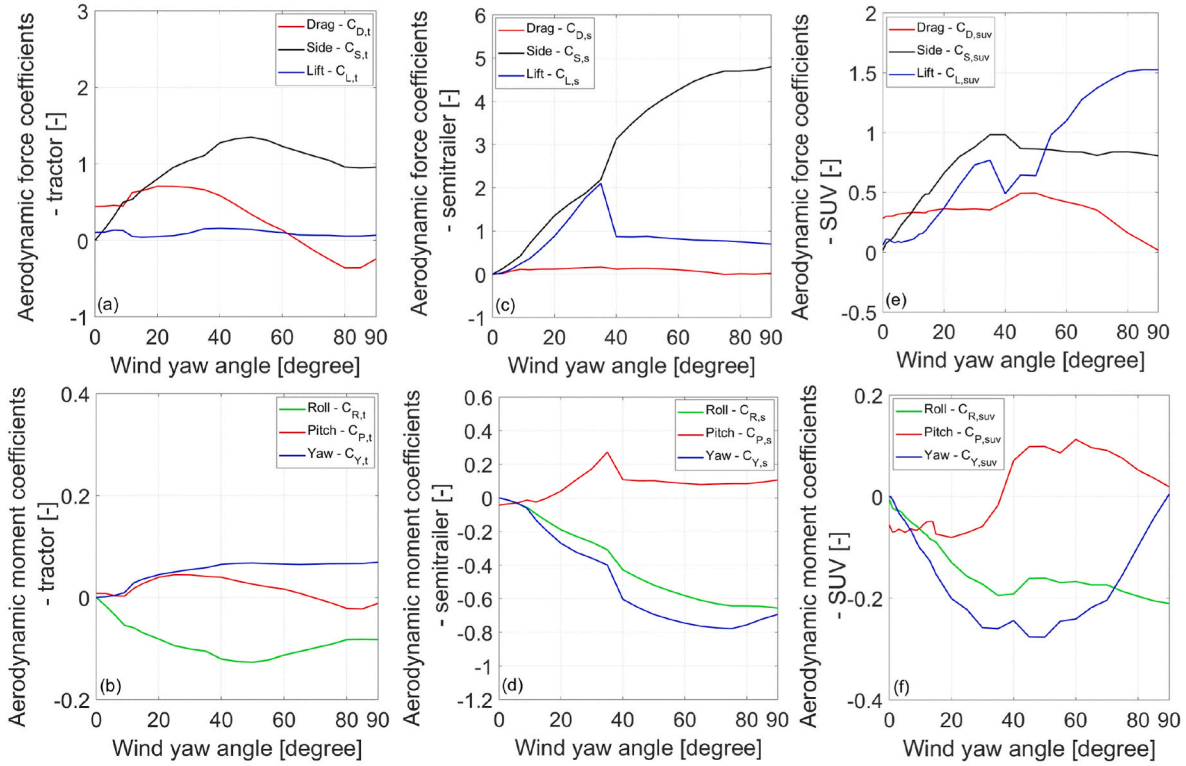

Fig. 11. Aerodynamic coefficients as a function of the wind yaw angle for a) forces (tractor); b) moments (tractor); c) forces (semitrailer); d) moments (semitrailer); e) forces (SUV); f) moments (SUV).

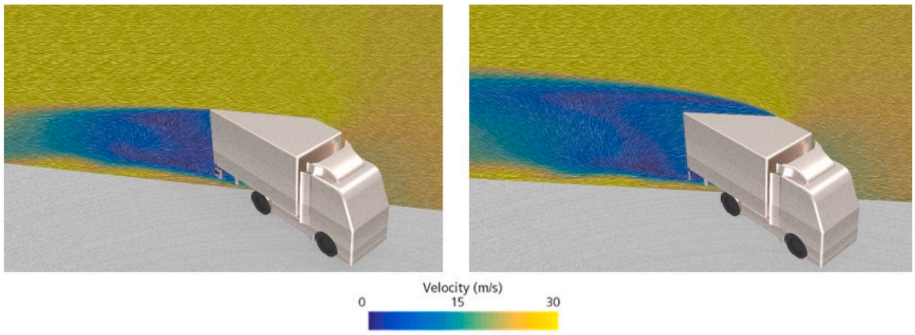

Fig. 12. Flow field comparison around the roof of a semitrailer at 35° (left) and 40° (right) of wind yaw angle.

$$M_{wind\ pitch,i} = (-1)\cdot\frac{1}{2}\rho V_{rel\ i}^2\cdot A_i\cdot L_i\cdot\left(c_{P,i}(\beta_{wi}) + R_{pitch\_i}\cdot c_{L,i}(\beta_{wi}) - \frac{h_{CoG,i}}{L_i}\cdot c_{D,i}(\beta_{wi})\right) \quad (34)$$

where $R_{pitch\_1} = \frac{l_{tf}}{L_t}$; $R_{pitch\_2} = -\frac{l_{s2}-l_{s3}}{L_s}$; $R_{pitch\_3} = -\frac{\frac{L}{2}-l_f}{L}$

$$M_{wind\ yaw,i} = \frac{1}{2}\rho V_{rel\ i}^2\cdot A_i\cdot L_i\cdot\left(c_{Y,i}(\beta_{wi}) + R_{yaw\_i}\cdot c_{S,i}(\beta_{wi})\right) \quad (35)$$

where. $R_{yaw\_1} = -\frac{l_{tf}}{L_t}$; $R_{yaw\_2} = \frac{l_{s2}-l_{s3}}{L_s}$; $R_{yaw\_3} = \frac{\frac{L}{2}-l_f}{L}$

In the aerodynamic equations, $i = 1,2,3$ refer to the tractor unit, semitrailer unit and SUV, respectively. $F_{xwind,i}$, $F_{ywind,i}$ and $F_{zwind,i}$ are the wind forces acting on the vehicle CoGs along the x_i-, y_i- and z_i-axes, respectively. $M_{wind\ roll,i}$, $M_{wind\ pitch,i}$ and $M_{wind\ yaw,i}$ are the wind moment components about the vehicle x_i-, y_i- and z_i-axes, respectively. $V_{rel\ i}$ is the relative wind velocity. A_i is a vehicle frontal area (where $A_1 = A_2$). L_i is the vehicle reference length (for the TS $L_1 = L_2$ and is equal to the total length of the combination; for the SUV, the wheelbase length is used as L_3). $c_{D,i}$, $c_{S,i}$, $c_{L,i}$, $c_{P,i}$, $c_{Y,I}$ and $c_{R,i}$ are vehicle aerodynamic coefficients that are functions of the wind yaw (attack) angle β_{wi}, and ρ is the air density.

For the relative wind velocity and wind yaw angle calculation, the same procedure as in (Sekulic, 2018) was used. It transforms the wind velocity signals from the global (Earth) coordinate system ($OXYZ$) into the vehicle coordinate system ($O_i x_i y_i z_i$; $i = 1,2,3$) (Fig. 15).

Fig. 16 shows the wind side force for each vehicle as a function of distance and five vehicle speeds. The semitrailer unit is exposed to the highest magnitude wind side forces due to its high side area. High values of the wind side force could cause large displacement of this unit from the path and lead to leaving the traffic lane.

Fig. 17 shows the wind rolling moment for the TS and SUV at five speeds as a function of distance. The semitrailer unit is exposed to the highest magnitude wind rolling moment. High values of the wind rolling moment, especially at high vehicle speeds, could cause a roll-over risk of this unit.

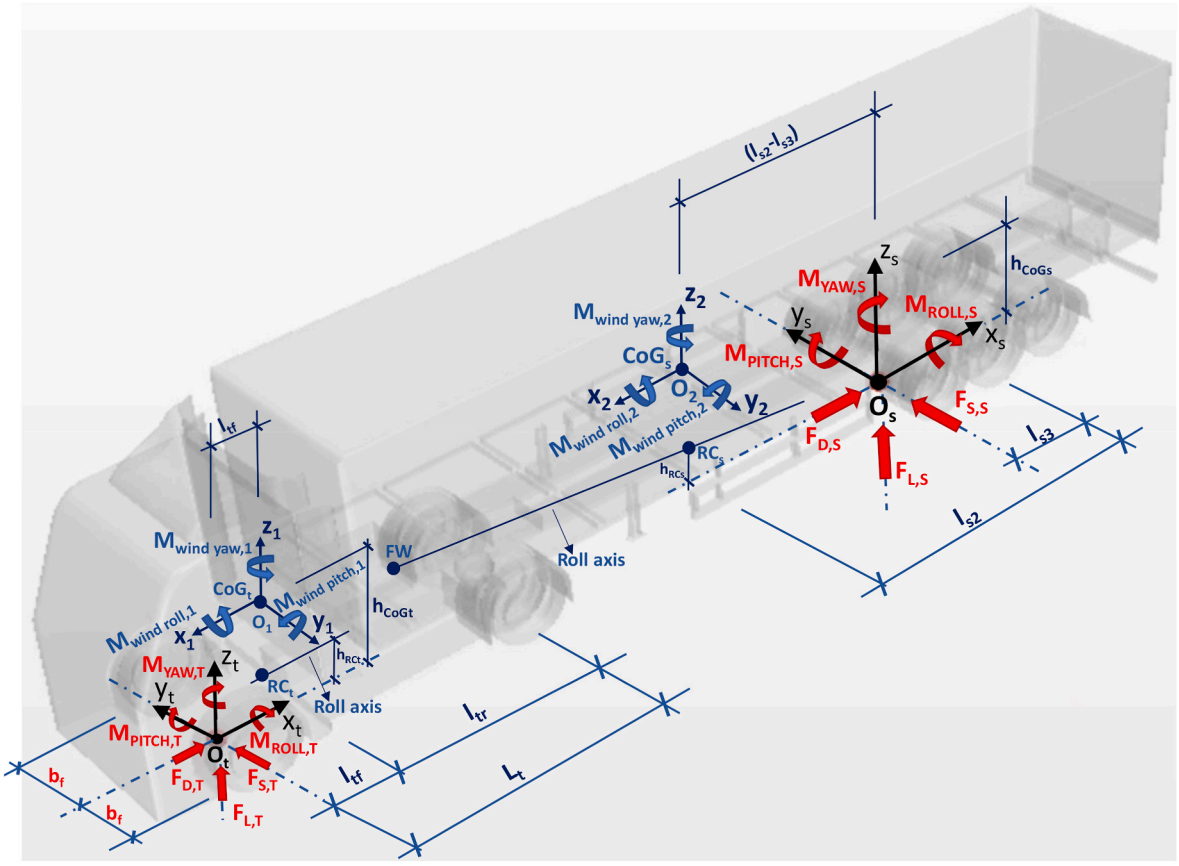

Fig. 13. Coordinate systems (ISO 4130, ISO 8855) for the TS model.

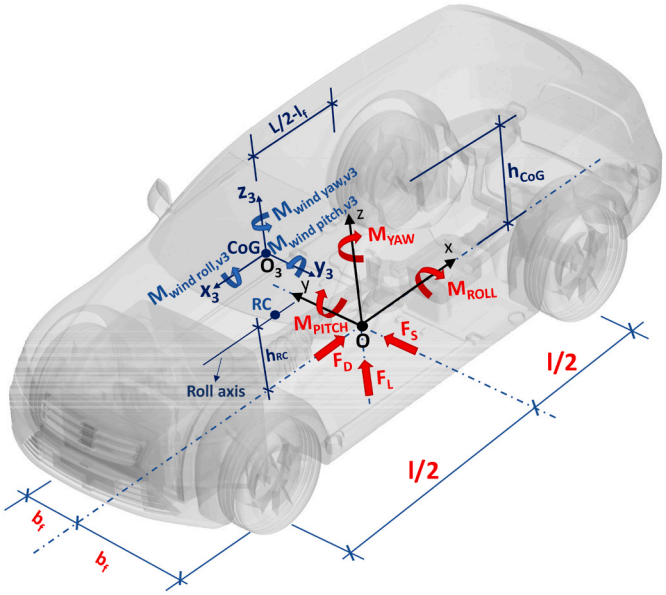

Fig. 14. Coordinate systems (ISO 4130, ISO 8855) for the SUV model.

3. Bridge model

Floating bridge was modelled as finite element model in *Orcaflex* software for dynamic analysis and *Sofistik* for static analyses (Vegvesen, 2017). An overview of how the floating bridge is modelled numerically (*Orcaflex* model) is given in Fig. 18.

The line elements used for describing the structural properties of the bridge applies finite segment theory, which yields similar results as using finite element beam theory for slender structures. The model considers geometric non-linear stiffness for each static position and each time step. For the mooring lines and stay-cables a different element is used, cables elements that have no stiffness in compression, bending or torsion. A master-slave connection is used between elements that are not directly connected.

The south abutment is fixed to the bridge girder in all 6 DOFs, while at the north abutment the bridge is free to elongate and to rotate about vertical axis. At the tower the bridge girder has a fixed connection for rotation, vertical translation, and horizontal translation. A linear material model is used for all elements.

The hydrodynamic loads and properties for the pontoons are given in the pontoon node at the water line. Hydrodynamic Morrison loads are defined for the mooring lines. Wind loads are applied for all objects above the water line, however for the pontoon only the static wind load is included.

4. Vehicle model excitations

Both vehicle models were excited with floating bridge vertical, lateral and roll motions as well as wind loads for 1-year storm conditions. The input data set is the same as those used for the bus model, and detailed information can be found in (Sekulic, 2018).

4.1. Bridge vertical excitation

Vertical excitations on the left and the right TS wheels are obtained by Eq. (36):

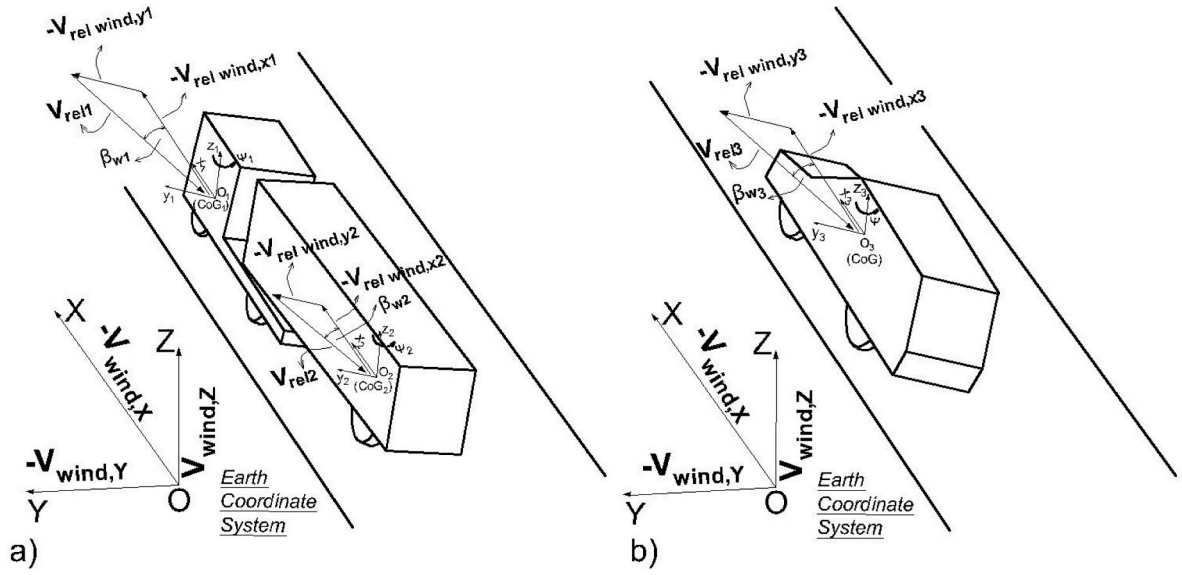

Fig. 15. Wind velocities in a) the Earth (OXYZ) and TS ($O_1x_1y_1z_1$, $O_2x_2y_2z_2$) coordinate systems; b) the Earth (OXYZ) and SUV ($O_3x_3y_3z_3$) coordinate system.

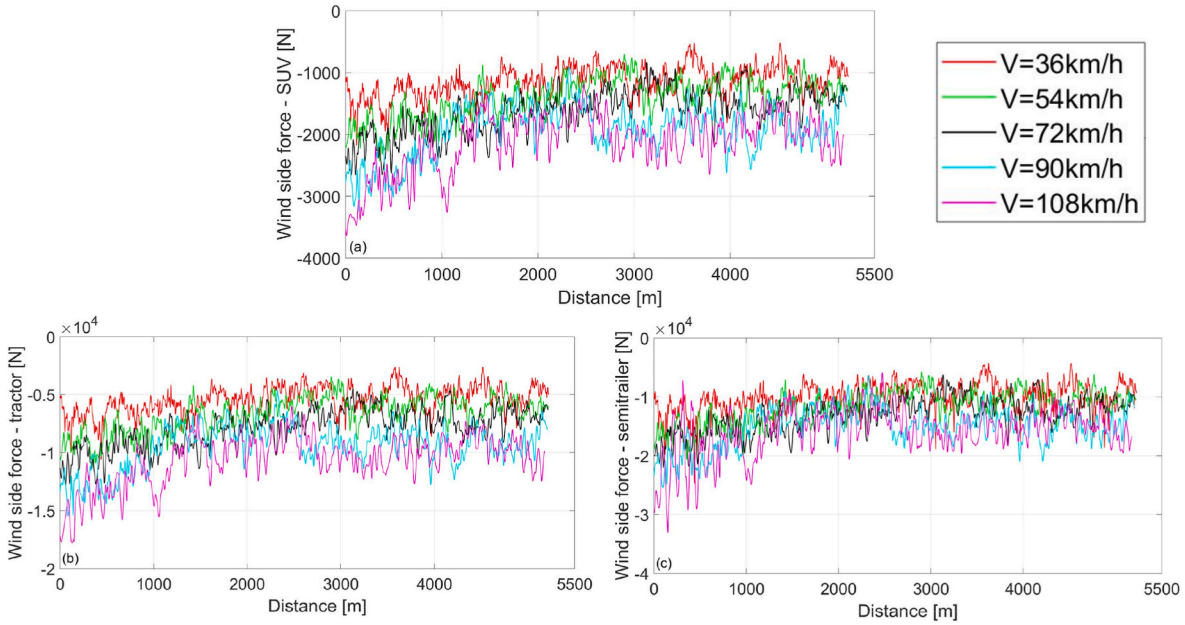

Fig. 16. Wind-side force as a function of distance and vehicle speed for a) the SUV; b) the tractor unit; c) the semitrailer unit.

$$\zeta_{w,i}(vt) = z_{br}(vt) + \zeta_{rr}(vt) + d_i \cdot \varphi_{br}(vt) = \zeta_R(vt) + d_i \cdot \varphi_{br}(vt),\ (i = tfl, tfr, trl, trr,\ sl,\ sr) \tag{36}$$

where $z_{br}(vt)$ is bridge vertical displacement (point C, Fig. 20a); $\zeta_{rr}(vt)$ is road roughness modelled by ISO 1995 8608 ISO, 1995; d_i is lateral distance from the rotational centre (point C) to the contact point between the TS wheel and the bridge deck (Fig. 20a); $\varphi_{br}(vt)$ is roll motion of the bridge deck; $\zeta_R(vt)$ is vertical excitations on the point R (Fig. 20a).

A random road profile can be represented by an infinite sum of harmonic functions of different amplitudes, circular frequencies and phase angles, according to Shinozuka (1972), Eq. (37)

$$\zeta_{rr}(x) = \sum_{i=1}^{N} A_i \cdot cos(2\pi \cdot n_i \cdot x + \alpha_i) \tag{37}$$

where N is number of harmonic waves; A_i is amplitude of harmonic waves in [m]; n_i is the discrete frequencies of excitation in [cycle/m]; α_i is the independent random phase angles uniformly distributed in the interval [0, 2 π]. Number of harmonics is $N = 1000$ according to (Sekulic et al., 2013).

Amplitude of harmonic waves is given by Eq. (38)

$$A_i = \sqrt{2 \cdot \Delta n \cdot \Phi_\zeta(n_i)} \tag{38}$$

where Δn is spatial frequency step in [cycle/m]; $\Phi_\zeta(n_i)$ is PSD of road elevation in [m^2/(c/m)];

ISO 8608 defines PSD by Eq. (39)

$$\Phi_\zeta(n) = \Phi_\zeta(n_0) \cdot \left(\frac{n}{n_0}\right)^{-w} \tag{39}$$

where $\Phi_\zeta(n_o)$ is PSD for reference spatial frequency (for A/B road class $\Phi_\zeta(n_o) = 32 \cdot 10^6$ [m^2/(c/m)] which is road in good condition); n_o is

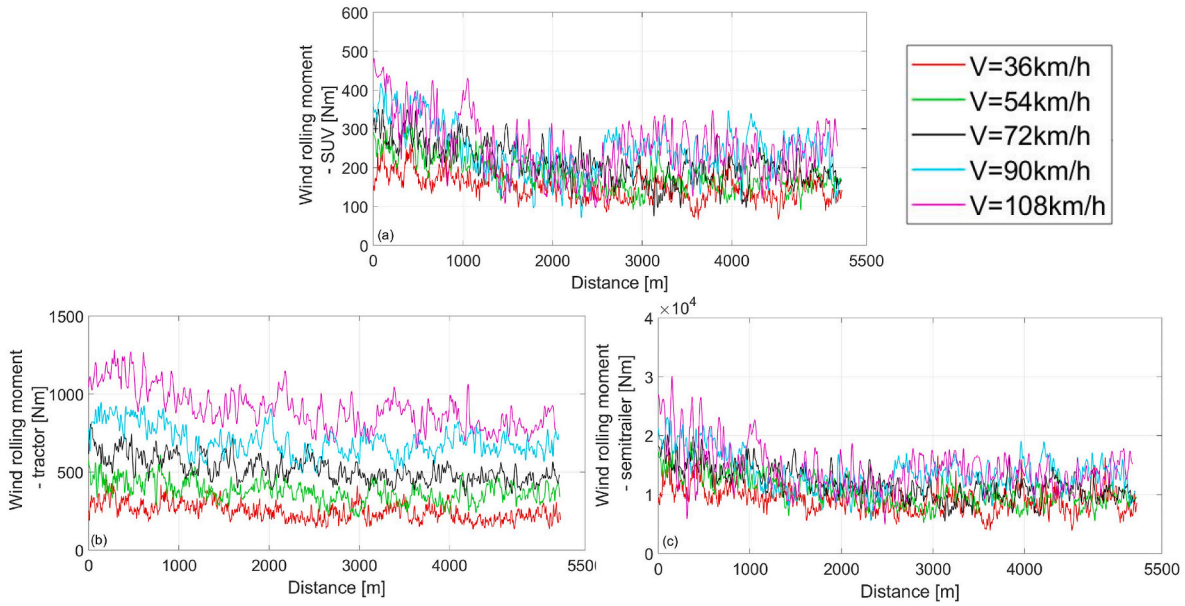

Fig. 17. Wind rolling moment as a function of distance and vehicle speed for a) the SUV; b) the tractor unit; c) the semitrailer unit.

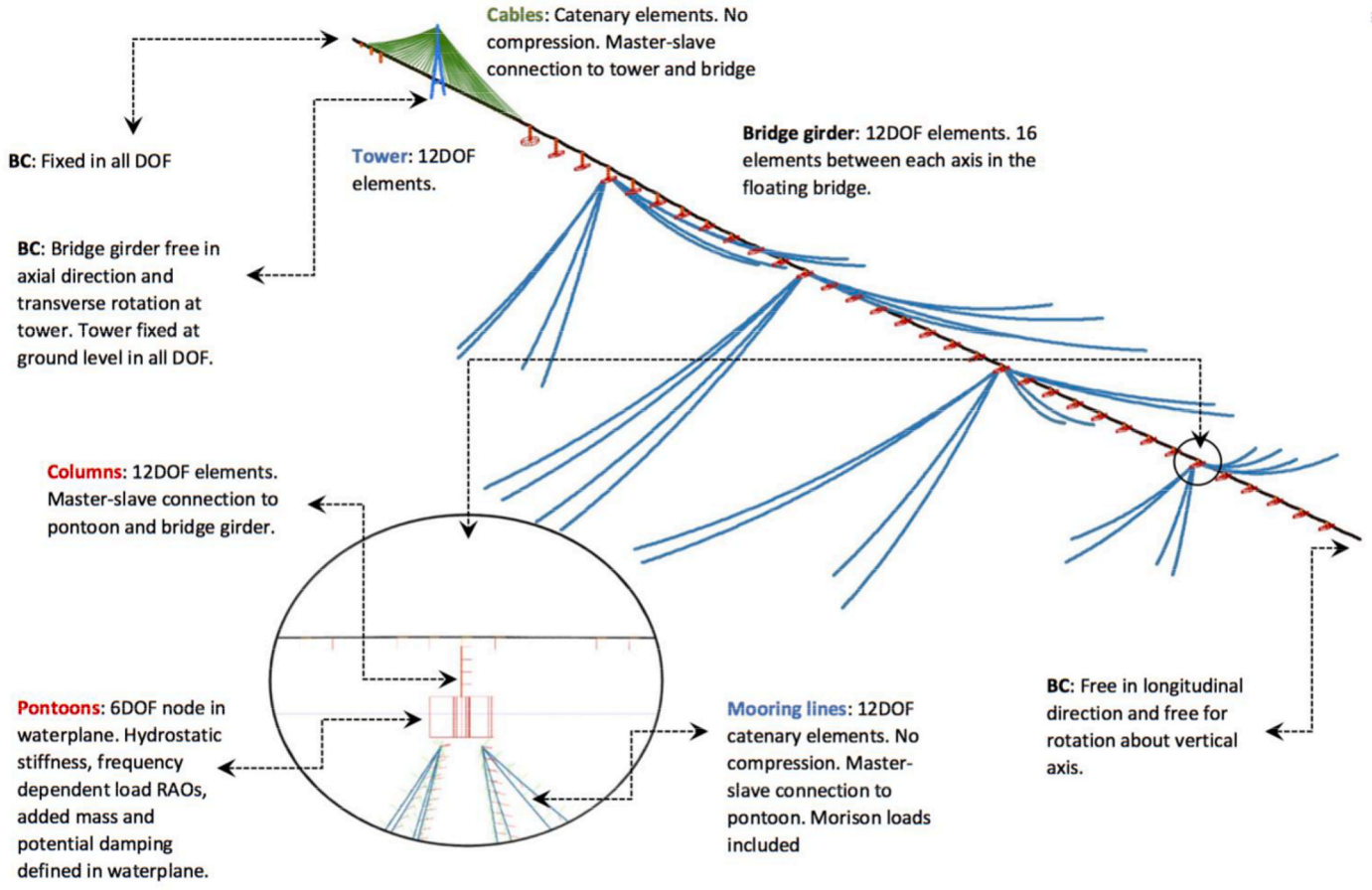

Fig. 18. Overview of Orcaflex model used for environmental analyses (Vegvesen, 2017).

reference spatial frequency ($n_0 = 0.1$ [c/m]); w is exponent of fitted PSD (w = 2);

Spatial frequency step is given by Eq. (40)

$$\Delta n = \frac{n_{max} - n_{min}}{N} \tag{40}$$

where n_{max} is maximum spatial frequency ($n_{max} = 2.83$ [c/m], according to ISO 1995 8608 ISO, 1995); n_{min} is minimum spatial frequency ($n_{min} = 0.011$ [c/m], according to ISO 1995 8608 ISO, 1995);

The length of the modelled A/B road is equal to the length of the Bjørnafjorden floating bridge (5240 m). Fig. 19a shows the road

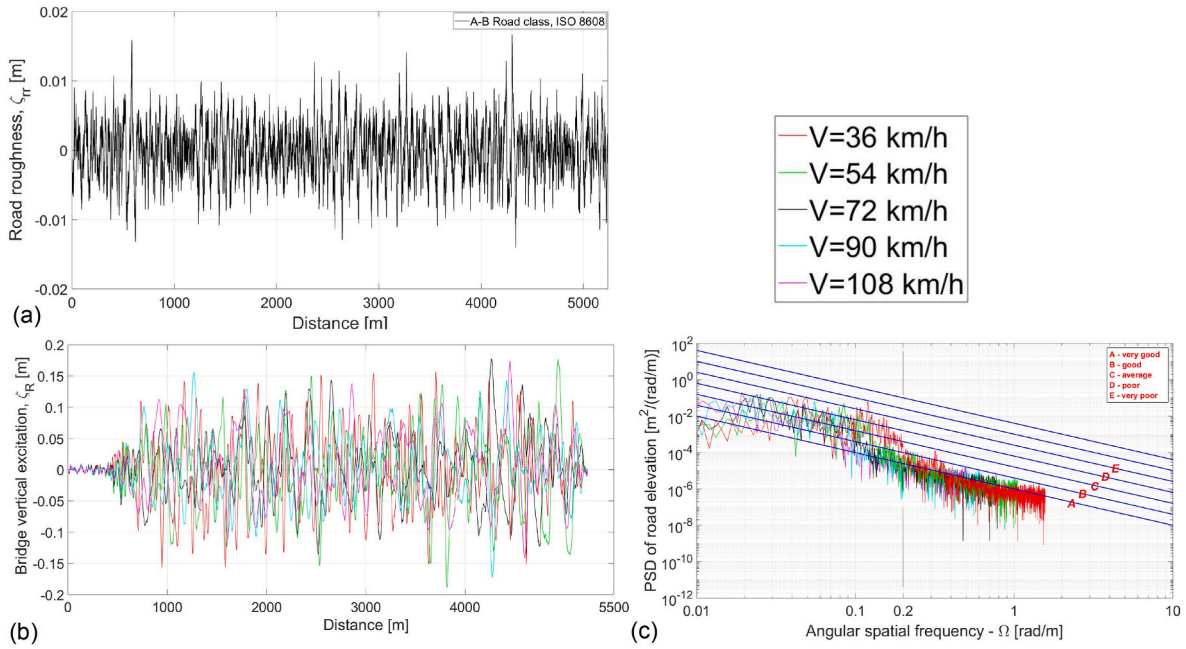

Fig. 19. Vertical excitation a) A/B road class generated from ISO 8608 standard; b) vertical bridge excitation (point R) as a function of distance and vehicle speed; c) PSDs of vertical floating bridge excitation in the ISO 8608 standard.

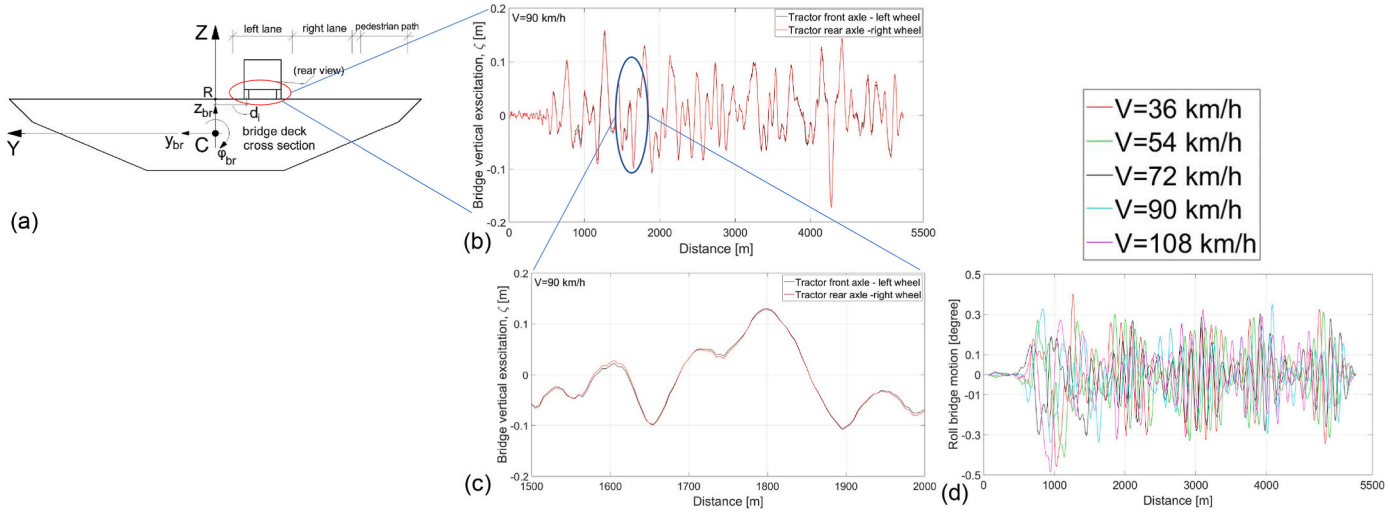

Fig. 20. a) Bridge deck cross section; b) vertical excitations on the left/right track for the left lane for a vehicle speed of 90 km/h; c) magnified view for the left/right track for a vehicle speed of 90 km/h; d) bridge roll motion as a function of distance and vehicle speed.

roughness as a function of distance. The roughness magnitudes are distributed mainly within ±0.01 m. Fig. 19b shows vertical excitations for the point R on the bridge deck (Fig. 20a) as function of bridge distance and vehicle speed. The vertical bridge excitation magnitudes are distributed mainly within ±0.2 m.

Fig. 19c presents vertical excitation in the ISO 8608 standard in function of spatial frequency. It could be noticed that bridge excitations with low angular spatial frequencies (long wavelengths) prevail. High PSDs exist at frequencies below 0.2 rad/m. Roughness at higher angular spatial frequencies (larger than 0.2 rad/m) mainly comes from the A/B road class that was modelled using ISO 8608. When moving across a floating bridge, vehicles will be vertically excited by the moving deck with low frequencies (e.g., even for the highest speed of 108 km/h, the frequencies are below 0.1 Hz (Sekulic, 2018)).

Fig. 20a shows TS left and right wheels on the bridge deck cross section. Fig. 20b shows an example for the left/right track vertical excitations for the left traffic lane as a function of time for a TS speed of 90 km/h. Fig. 20d shows roll-angle bridge motion data as a function of time for five different vehicle speeds. The roll motions for each bus speed are small, within ±0.5°. Vertical bridge excitations for the right traffic lane are considered to be identical to vertical excitations for the left traffic lane due to insignificant bridge roll motion values.

4.2. Bridge lateral excitation

The lateral bridge velocities were used as inputs when calculating the lateral tire slip for lateral tire forces (Eqs.27–29). Lateral bridge motions were used as inputs for the vehicle driver model when calculating the handwheel steering angles. Fig. 21a presents the lateral bridge motion for a vehicle front axle as a function of distance and vehicle velocity. The bridge lateral displacement values lie within ±0.1 m. Fig. 21b presents the PSD of the bridge lateral displacement as a function of different

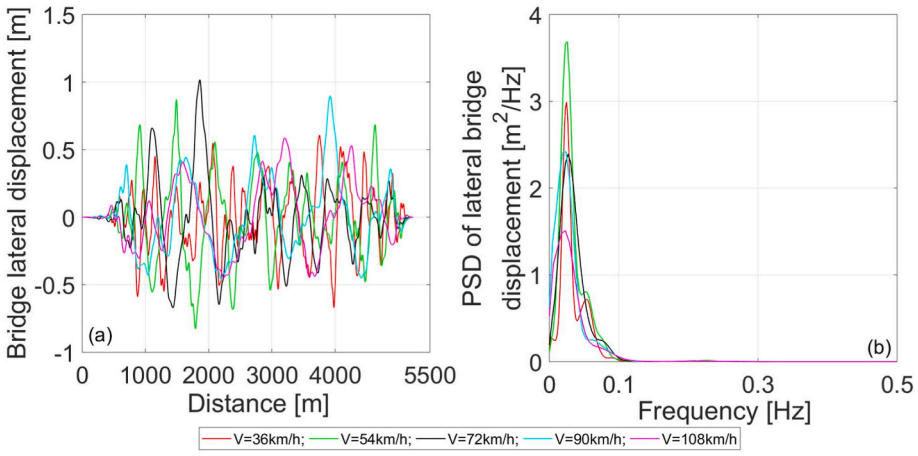

Fig. 21. Lateral bridge displacement for different vehicle velocities as a function of a) distance; b) frequency.

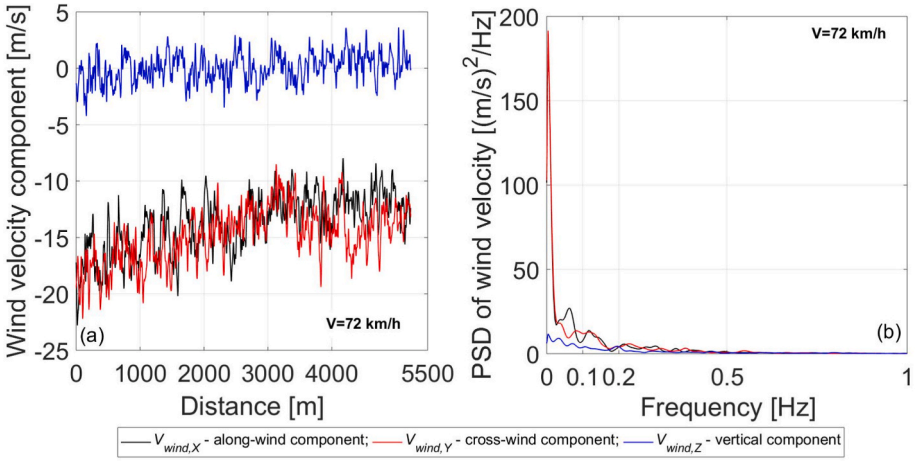

Fig. 22. Wind velocity components for a vehicle velocity of 72 km/h as a function of a) distance; b) frequency.

vehicle speeds. The lateral bridge motion intensities go below 0.1 Hz, and these excitation frequencies correspond to the excitation frequencies of the crosswind component (Fig. 22b).

The roll motion for each vehicle speed is small, within ±0.5° (Sekulic, 2018). This motion has been incorporated as an input through the vertical excitations on the vehicle left/right tracks.

4.3. Wind excitations

A stochastic wind velocity field was generated in *WindSim* software (Vegvesen, 2017). Turbulent wind time series are simulated in the *WindSim* code for a set of positions based on mean wind speed, single point gust spectrum and coherence functions. The code is using inverse FFT (the fast Fourier transform) to generate the wind speed time series from a spectral description of the fluctuating wind components.

The mean wind speed is defined in the design basis as the 1-h average at 10 m above sea level. The vertical wind profile is described by Eq. (41)

$$U(z) = U_{10} \cdot \left(\frac{z}{10}\right)^{\alpha} \tag{41}$$

where U_{10} is the mean wind speed at 10 m height; α is the profile factor of the wind profile (α is defined as 0.127 in the metocean report (Vegvesen, 2017)).

The turbulence spectrum as function of frequency n and integral length scale L_i is defined by Eq. (42) (according to N400 (Vegvesen, 2015) for wind components $i = u,v,w$, (u - longitudinal; v - transversal; w - vertical)):

$$\frac{nS_i}{\sigma_i^2} = \frac{A_i \hat{n}_i}{(1 + 1.5A_i\hat{n}_i)^{5/3}} \tag{42}$$

where A_i is integral length scale factors ($A_u = 6.48$; $A_v = A_w = 9.4$); $\hat{n}_i$ – is frequency given by Eq. (43)

$$\hat{n}_i = \frac{n\,L_i(z)}{U(z)} \tag{43}$$

where $L_i(z)$ is integral length scale. The integral length scale is 132 m calculated in accordance with N400 (Vegvesen, 2015) at the reference height.

The coherence function is an exponential decay function defined by Eq. (44)

$$\sqrt{coh(n\Delta S)} = exp\left(-C_i\frac{n\Delta S}{U(z)}\right) \tag{44}$$

where C_i is the decay factor for each wind component ($C_u = 10$; $C_v = C_w = 6.5$).

Fig. 22 presents an example of the wind velocity signal defined in the GCS for a vehicle speed of 72 km/h. The along-wind and crosswind components have larger magnitudes (close to 20 m/s) in the first 1000 m of the distance travelled and decrease to approximately 15 m/s at the end of the bridge. Fig. 22b presents the PSDs of the wind velocity components. Signal intensities are mainly concentrated in the low-

frequency range, below 0.1 Hz.

Simulation of bridge motions under the influence of environmental loads (wind and waves for 1-year storm conditions) was performed for 1 h (3600 s) of simulation time. A wind field was generated from a Kaimal wind spectrum with mean wind speed $w_s = 21.40$ m/s and along turbulence $I_u = 0.15$. The structure was excited by waves generated from a Jonswap spectrum with significant wave height ($H_s = 1.2$ m) and peak period ($T_p = 4.26$ s). Small swell waves propagating into the fjord from the North-Sea were also considered ($H_s = 0.22$ m, $T_p = 17$ s) (Vegvesen, 2017).

5. Driver model

The driver model based on the path tracking pure pursuit method previously defined in (Sekulic, 2018) was used for simulations in this work. When tuning the pure pursuit controller, a look-ahead time (LAT) of 0.6 s for heavy vehicles was confirmed (Sekulic, 2018). The same procedure was used here when determining a LAT for an SUV. Briefly, a LAT was defined by comparing the HSA responses from the tests (Bhat, 2020) performed on a driving simulator (CASTER) and numerical simulations.

Fig. 23 compares HSAs from driving simulator tests (two drivers) at a simulated speed of 72 km/h for the case of a LAT equal to 0.5 s. Although the magnitudes of the signals are similar (Fig. 23a–b), the frequencies are different (Fig. 23c). However, the HSA incorporates signal frequencies from both drivers (Fig. 23a). A LAT of 0.5 s is also confirmed for a vehicle speed of 90 km/h.

6. Simulation results and discussion

In this section, suggested measures for safe vehicle speeds for safe crossing Bjørnafjorden floating bridge will be presented. These measures have been proposed in (Sekulic, 2018). In addition, the results for the vehicle leaving the traffic lane will be discussed here. Simulation results refer to one specific driving condition (1-year storm condition; dry/wet asphalt (road friction of 0.7)) and two vehicle types. Proposed measures could also be applicable for different storm and road conditions and different vehicle types.

6.1. Risk of lateral path departure and leaving the traffic lane

6.1.1. Path tracking or lateral path deviation

This section presents simulation results for the path tracking of the TS and SUV. Path tracking reflects vehicle deviations from the path that vehicle is supposed to follow. Lateral distance between the vehicle CoG and the path (centreline within traffic lane) has been considered as the measure for path tracking. Small lateral distance means better path tracking, and vice versa. Fig. 24 shows lateral displacements for two vehicle models within traffic lane.

Fig. 25a–c shows the TS path tracking for velocities of 36 km/h, 90 km/h and 108 km/h. The deviation from the path increases for both units with the speed. Due to the crosswind load, the lateral offset from the path can be noticed for the semitrailer unit. At a speed of 108 km/h, the lateral displacement from the path is very large for both units when the vehicle enters the bridge (for a tractor up to 1.5 m and for a semitrailer up to 2.5 m). Fig. 25d shows the path tracking without wind acting on the vehicle but with bridge motion excitations for a vehicle velocity of 90 km/h. In this case, both units follow the path, and only minor lateral displacement of the semitrailer unit can be noticed.

Fig. 25e–f shows the path tracking for the SUV at speeds of 90 km/h and 108 km/h. At a speed of 90 km/h, in the case when the wind does not act, the vehicle follows the driving path (Fig. 25f). At a speed of 108 km/h, the vehicle path deviation is over 0.5 m when the vehicle enters the bridge (Fig. 25e).

6.1.2. Leaving the traffic lane

Under a crosswind, the lateral displacement from the vehicle path increases with the vehicle speed, and it is important to analyse whether the vehicle leaves the traffic lane. Fig. 26 shows the vehicles outermost points for which positions within traffic lanes will be analysed. Some important vehicle parameters, such as the total length (L_{TS}, L_{SUV}), total width (W_T, W_S, W_{SUV}) and front/rear overhangs (f_{oh_t}, r_{oh_s}, f_{oh_suv}, r_{oh_suv}), are also denoted in the same figure. Values of these parameters are given in Table 3.

Fig. 27 shows the position of the outermost body points for the semitrailer unit, tractor unit and SUV within the traffic lane. At a speed of 36 km/h, the outermost point at the rear-right side of the semitrailer only slightly leaves the traffic lane at distances of approximately 1 km and 4 km (Fig. 27a). At a speed of 72 km/h, the outermost point at the right/left sides of the semitrailer leave the traffic lane (rear-right side at distances of approximately 1,3 km and 2 km; front-left side at a distance of approximately 2 km, Fig. 27b). At a speed of 90 km/h, the semitrailer leaves the traffic lane more frequently (Fig. 27c). At a speed of 90 km/h, the outermost points at the left side of the tractor slightly leave the traffic lane close to 4 km of travelled distance (Fig. 27d).

At a speed of 90 km/h, the SUV stays in the traffic lane (Fig. 27e). At a speed of 108 km/h, the outermost points at the right side of the vehicle slightly leave the traffic lane after the vehicle enters the bridge

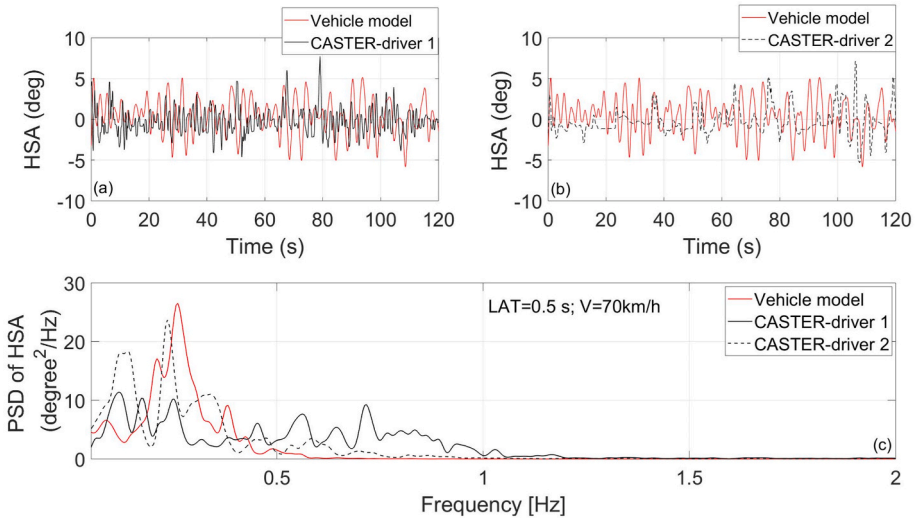

Fig. 23. HSA signals for an SUV and LAT = 0.5 s as a function of a) time (driver 1); b) time (driver 2); c) frequency.

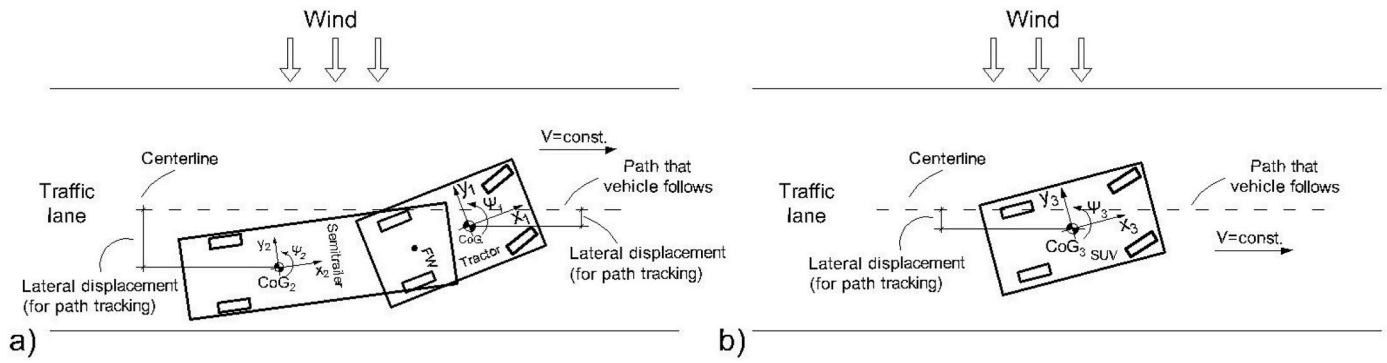

Fig. 24. Lateral displacement for path tracking analysis a) TS; b) SUV.

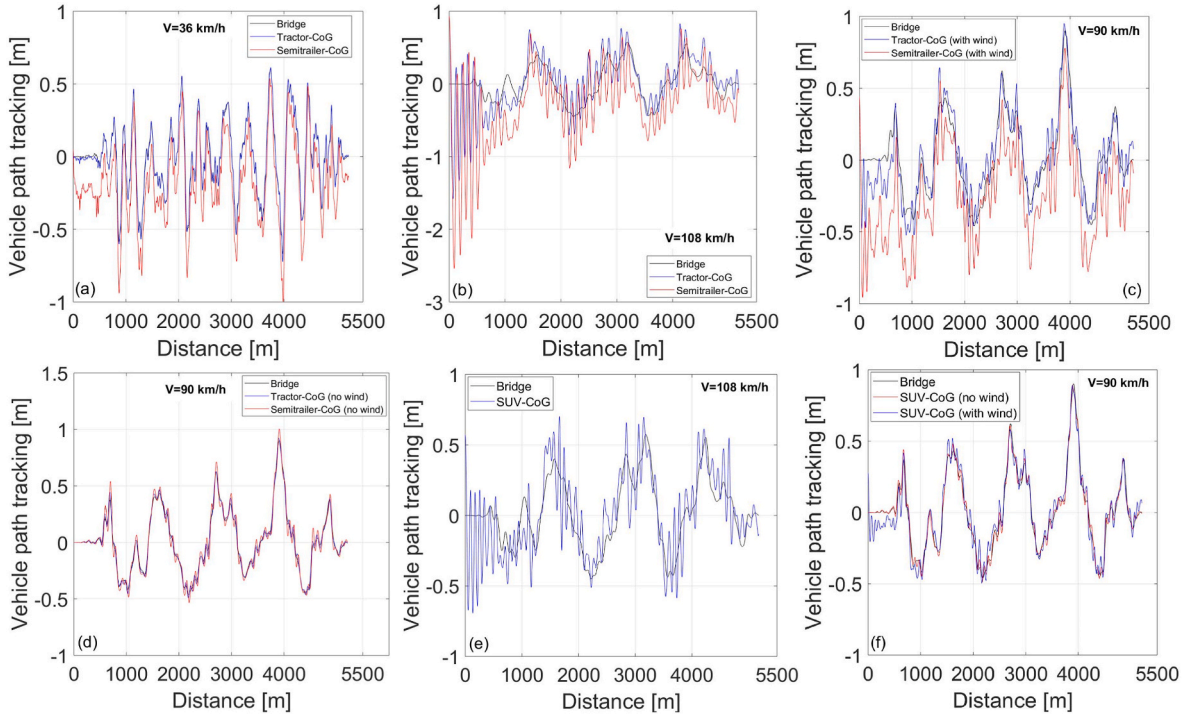

Fig. 25. Path tracking at velocities of a) 36 km/h for the TS; b) 108 km/h for the TS; c) 90 km/h (with wind) for the TS; d) 90 km/h (no wind) for the TS; e) 108 km/h for the SUV; f) 90 km/h for the SUV.

(Fig. 27f).

6.2. Driver steering effort

Fig. 28a–c presents the HSA as a function of distance for the TS and SUV. The HSA is of higher intensities for the TS than for the SUV. The HSA magnitudes for speeds of 36 km/h and 108 km/h for the SUV are similar. Fig. 28b–d shows the PSDs of the HSA signals for both vehicles. The intensities of the HSA are below 0.5 Hz, and concentrated into two frequency ranges, 0–0.1 Hz and 0.2–0.3 Hz. Intensities below 0.1 Hz are due to the excitations (crosswind (Fig. 22b) and lateral bridge displacement (Fig. 21b)) that the driver needs to compensate for. HSA intensities in the frequency range 0.2–0.3 Hz comes from the driver's compensation of the vehicle yaw moment caused by the generation of a tire lateral forces due to the lateral bridge velocity (Fig. 9b).

When driving across the floating bridge under the influence of cross-wind loads vehicle lateral displacement from the path will be larger when comparing it with the case when cross-wind is not present. Apparently more intensive driver inputs will be necessary to keep the vehicle on the path. Driver model which is based on pure pursuit tracking method confirms this when looking into HSA signal (Fig. 29). It could also be seen that intensive driver's steering wheel input is necessary to compensate for the cross-wind load and to steer the vehicle back on the path when vehicle enters the bridge section (Fig. 29).

6.3. Roll-over risk

Fig. 30 shows the total vertical force for each TS wheel as a function of time at a speed of 108 km/h. The vertical tire forces change considerably for the semitrailer unit due to the high value of the wind rolling moment acting on this unit (Fig. 17c). At a speed of 108 km/h, the windward wheel on the semitrailer axle loses contact with the bridge deck at, 6 s and 13 s (180 m and 380 m after the vehicle enters the bridge). Losing contact indicates a roll-over risk of the semitrailer unit and apparently of the whole vehicle. The roll-over risk for the semitrailer unit is also confirmed with the load transfer ratio (LTR) parameter, Fig. 30c.

Fig. 30d–e shows the vertical tire forces for the SUV at speeds of 90 km/h and 108 km/h. At both speeds, the wheels do not lose contact with the bridge deck. The vertical tire forces do not considerably change as in

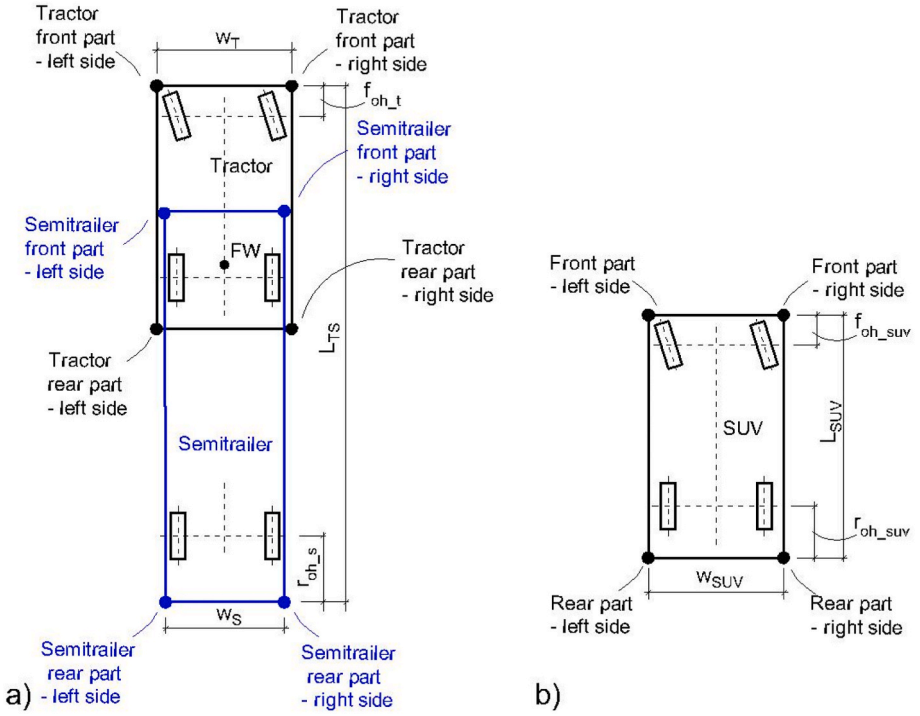

Fig. 26. Vehicle outermost body points for a) the TS; b) the SUV.

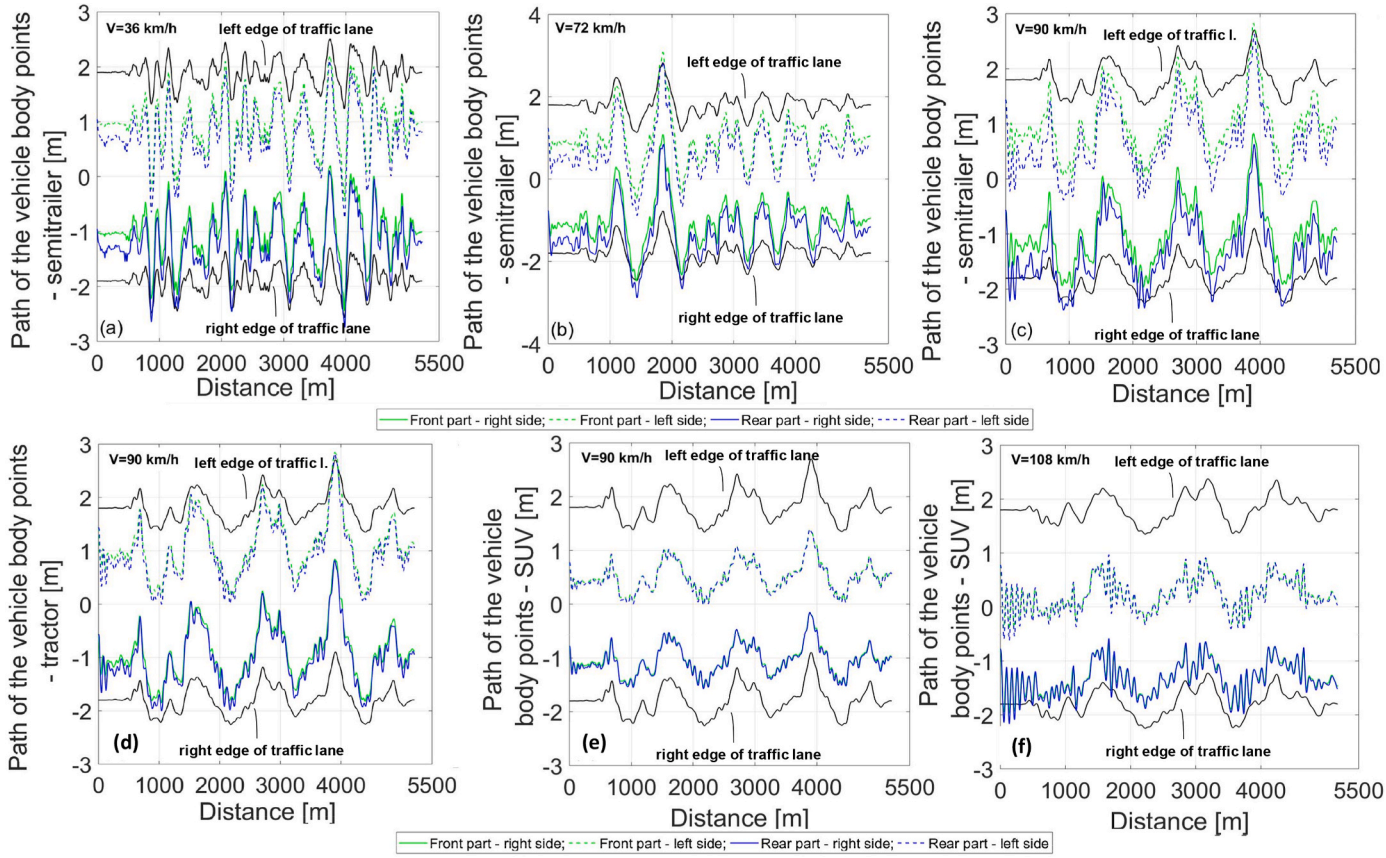

Fig. 27. Path of the outermost body points at velocities of a) 36 km/h for the semitrailer; b) 72 km/h for the semitrailer; c) 90 km/h for the semitrailer; d) 90 km/h for the tractor; e) 90 km/h for the SUV; f) 108 km/h for the SUV.

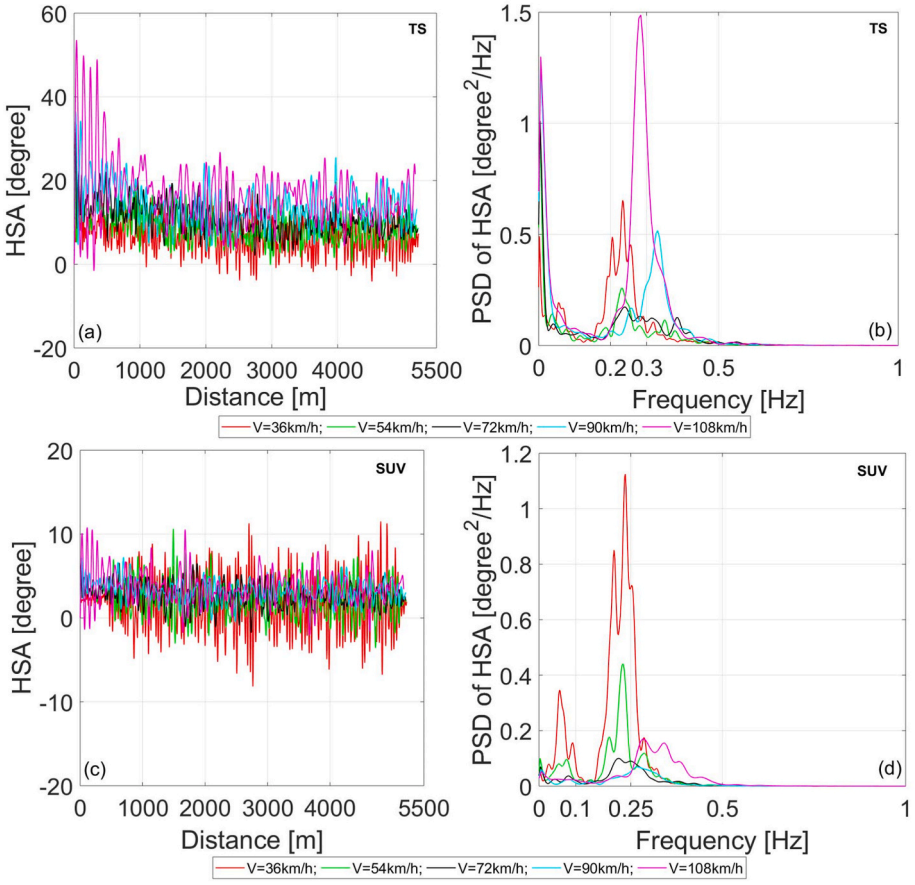

Fig. 28. HSA for different vehicle speeds as a function of a) distance for the TS; b) frequency for the TS; c) distance for the SUV; d) frequency for the SUV.

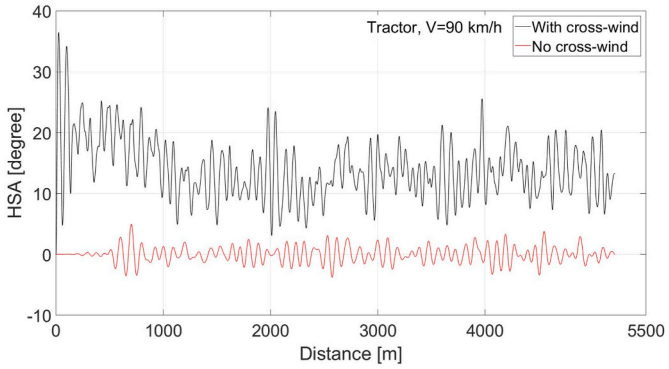

Fig. 29. HSA signal for tractor unit with cross-wind and without cross-wind component for the vehicle speed of 90 km/h.

the case of the TS vehicle due to the much lower height of the SUV's CoG and independent suspension system.

6.4. Comparisons of the proposed measures for the TS and SUV

6.4.1. RMS value and maximum absolute value for path deviation

Fig. 31 shows the simulation results for the path deviation of both vehicles as a function of vehicle speed. The path deviation increases with the vehicle speed (Fig. 31a). The RMS value of the path deviation is the highest for the semitrailer unit. The RMS values are similar for the tractor unit and SUV at a velocity range of 36–54 km/h. The maximal deviation increases with the vehicle velocity, and the semitrailer unit reaches a high value of 2.5 m at a speed of 108 km/h. The maximal deviation is below 0.5 m for the semitrailer unit, tractor unit and SUV at velocities lower than 60 km/h, 90 km/h and 100 km/h, respectively (Fig. 31b).

6.4.2. Mean value and RMS value of the HAS

Fig. 32 shows the mean and RMS value of the HSA for the TS and SUV. Mean and RMS values increase with the vehicle velocity. These parameters have higher values for the TS than for the SUV. According to the simulation results, the TS driver would experience more effort in vehicle handling over the floating bridge compared to the SUV driver.

6.4.3. Maximum of absolute and RMS value of LTR parameter

Fig. 33 shows the maximum absolute LTR value for the TS and SUV as a function of velocity. A roll-over risk (a LTR higher than 0.9) is indicated for the semitrailer unit at speeds greater than 95 km/h (Fig. 33a). No roll-over risk is noticeable for the SUV (the LTR value is considerably lower than 0.9, Fig. 33b).

Fig. 34 shows the RMS value of the LTR parameter. The RMS value increases with the vehicle velocity. High RMS values for the semitrailer axle indicate a vehicle roll-over risk due to wheel lift-off (Fig. 34a). The RMS value is considerably lower for the SUV than for TS (below 0.03, Fig. 34b).

6.4.4. Minimum value of the LSL parameter

Fig. 35 shows the minimum value of the LSL parameter for the TS and SUV as a function of velocity. The LSL value decreases with vehicle velocity. LSL values are greater than zero for each axle/vehicle, indicating that for the considered road surface (dry/wet road), no sideslip risk is noticeable. The SUV rear axle has the lowest LSL value at a speed of 108 km/h (Fig. 35b).

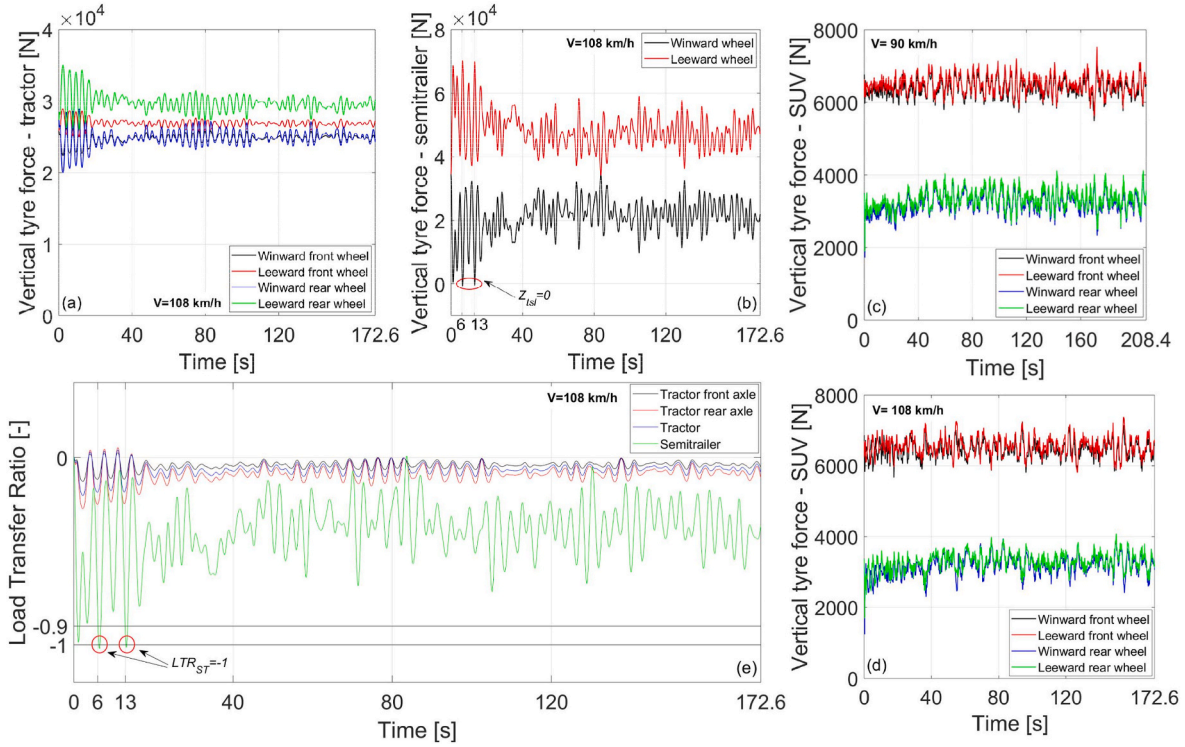

Fig. 30. Vertical tire forces for a) the tractor (speed of 108 km/h); b) the semitrailer (speed of 108 km/h); c) the SUV (speed of 90 km/h); d) the SUV (speed of 108 km/h) and the LTR for e) the TS (speed of 108 km/h).

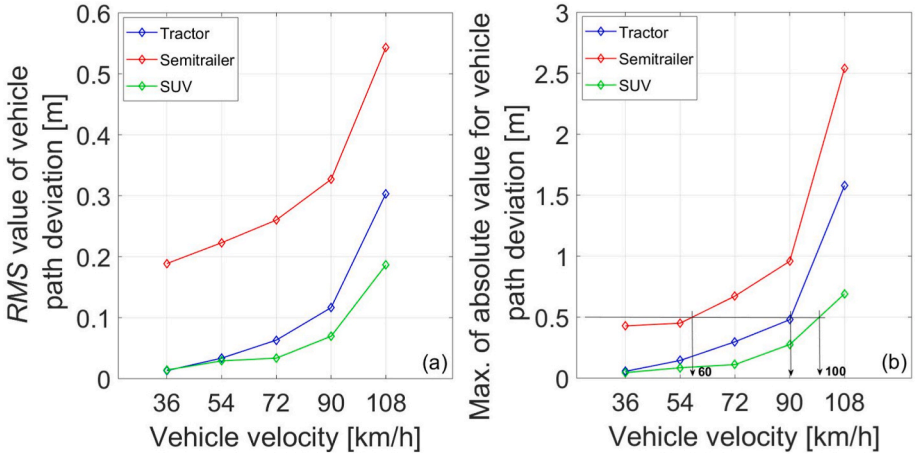

Fig. 31. Path deviation a) RMS value; b) maximum of the absolute value.

7. Conclusion

In this work, vehicle dynamic models for two vehicle types, a TS and an SUV, were defined for the analysis of vehicle/driver behaviour and safe speed recommendations for the Bjørnafjorden floating bridge in Norway considering a 1-year storm condition.

From this research, the main conclusions are as follows:

- The vehicle lateral displacement from the path increases with increasing vehicle speed. The lateral displacement is large for the tractor/semitrailer combination when entering the bridge (for a tractor unit up to 1.5 m and for a semitrailer unit up to 2.5 m) at a speed of 108 km/h. For the SUV, the path deviation is slightly over 0.5 m when entering the bridge.
- The crosswind load influences vehicle path deviation the most. Considering floating bridge motions separately, these motions do not have a substantial influence on the vehicle's path tracking ability.
- At a speed of 90 km/h, the tractor unit slightly leaves the traffic lane at only one position (at a distance of approximately 4 km) on the bridge. At speeds of 36 km/h and 72 km/h, the semitrailer unit slightly leaves the traffic lane at a few positions on the bridge. At a speed of 90 km/h, the semitrailer unit leaves the traffic lane more frequently and more severely along the bridge.
- At a speed of 90 km/h, the SUV stays in the traffic lane. At a speed of 108 km/h, the outermost points on the SUV right side leave the traffic lane after the vehicle enters the bridge.
- The roll-over risk (a LTR higher than 0.9) is indicated for the semi-trailer unit at speeds greater than 95 km/h. No roll-over risk is noticeable for SUV (the LTR value is considerably lower than 0.9).

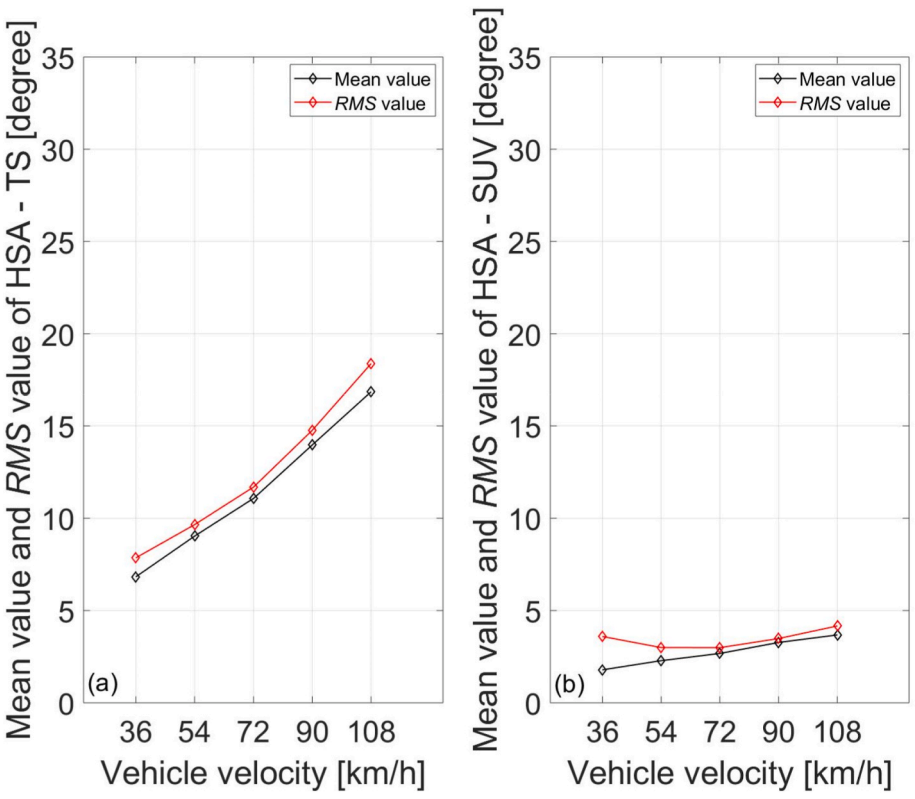

Fig. 32. Mean and RMS value of the HSA for a) the TS; b) the SUV.

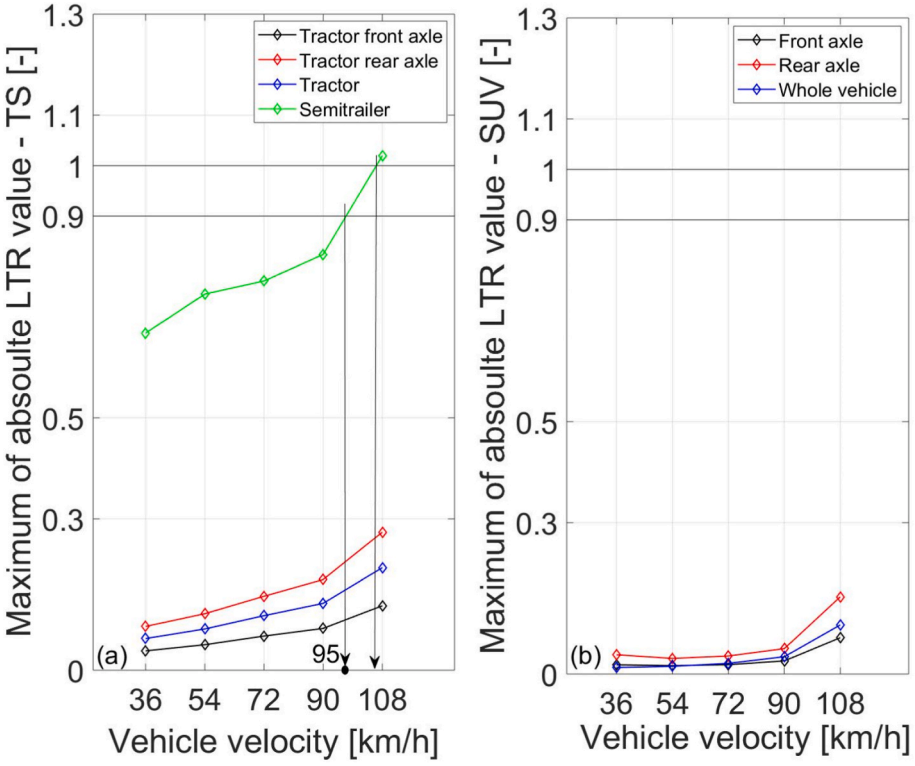

Fig. 33. Maximum absolute LTR value for a) the TS; b) the SUV.

- According to the simulation results, the TS driver would require more effort for vehicle handling over the floating bridge compared to the SUV driver.
- The LSL values are greater than zero for each axle/vehicle, indicating that for the considered road surface (dry/wet road), no sideslip risk is noticeable.

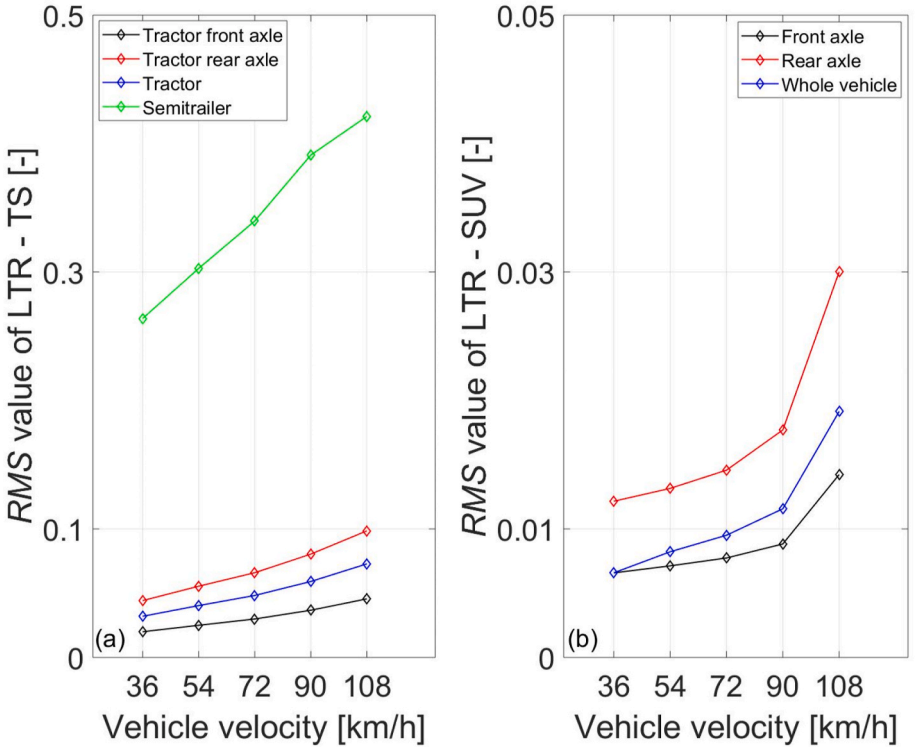

Fig. 34. RMS value of the LTR for a) the TS; b) the SUV.

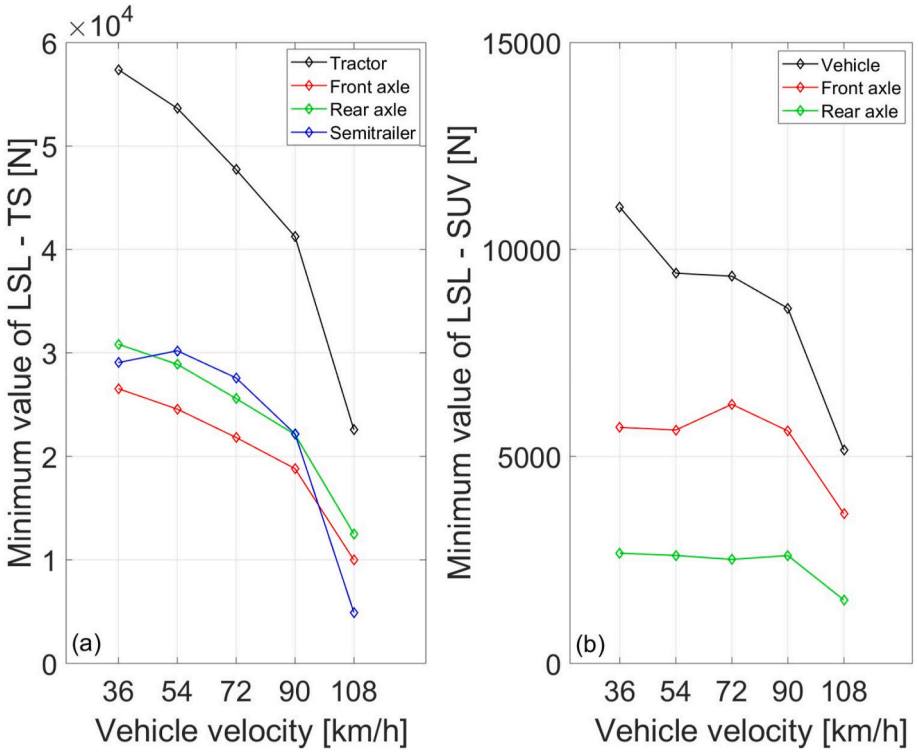

Fig. 35. Minimum value of the LSL for a) the TS; b) the SUV.

- The simulation results suggest that a TS could safely enter the bridge at a low speed (36 km/h) and increase speed up to 72 km/h after travelling 2 km. An SUV could safely enter the bridge at a speed of 90 km/h and increase the speed up to 108 km/h after travelling 0.5 km.

CRediT authorship contribution statement

Dragan Sekulic: Conceptualization, Methodology, Data curation, Visualization, Writing – original draft, preparation, Writing – review & editing. **Alexey Vdovin:** Supervision, Conceptualization, Writing –

review & editing. **Bengt Jacobson:** Supervision, Conceptualization, Methodology, Validation. **Simone Sebben:** Supervision, Conceptualization, Writing – review & editing. **Stian Moe Johannesen:** Investigation, Resources, Writing – review & editing.

Declaration of competing interest

The authors declare that they have no known competing financial interests or personal relationships that could have appeared to influence the work reported in this paper.

Data availability

Data will be made available on request.

Acknowledgements

Support for this research was provided by The Norwegian Public Roads Administration (NPRA). This support is gratefully acknowledged. The aerodynamic simulations were performed on resources provided by the Swedish National Infrastructure for Computing (SNIC).

Appendix

Table 1
Tractor-semitrailer parameters

Geometric parameters of the tractor/semitrailer unit	
Tractor wheelbase, L_t [m]	5.95
Distance from the tractor front axle to its CoG, l_{ft} [m]	3.00
Distance from the tractor rear axle to its CoG, l_{rt} [m]	2.95
Distance from the tractor front right/left wheel to the front axle CoG, b_f [m]	1.00
Distance from the tractor rear right/left wheel to the rear axle CoG, b_r [m]	1.00
Distance from the tractor CoG to the ground, $h_{CoG,t}$ [m]	1.16
Distance from the tractor CoG to the fifth wheel, a [m]	2.75
Height of the tractor roll-centre, h_{RCt} [m]	0.6306
Height of the tractor front axle roll-centre, $h_{RCfa.}$ [m]	0.6306
Height of the tractor rear axle roll-centre, $h_{RCra.}$ [m]	0.6306
Distance from the tractor CoG to the roll-centre of the front axle, Δh_{sf} [m]	0.5294
Distance from the CoG to the roll-centre of the rear axle, Δh_{sr} [m]	0.5294
Distance from suspension elements on the tractor front axle to the front axle CoG, e_{u1} [m]	0.70
Distance from suspension elements on the tractor rear axle to the rear axle CoG, e_{u2} [m]	0.80
Semitrailer wheelbase, L_s [m]	11.08
Distance from the fifth wheel to the semitrailer CoG, l_{s1} [m]	9.18
Distance from the semitrailer axis to its CoG, l_{s2} [m]	1.19
Distance from the semitrailer right/left wheel to its axle CoG, b_s [m]	1.00
Distance from the semitrailer CoG to the ground, $h_{CoG,s.}$ [m]	1.724
Height of the semitrailer axle roll-centre, $h_{RCsa.}$ [m]	0.6306
Distance from the semitrailer CoG to the roll-centre for its axle, Δh_{ss} [m]	1.0934
Height of the semitrailer roll-centre, h_{RCs} [m]	1.0765
Distance from suspension elements on the semitrailer axle to its CoG, e_{us} [m]	0.80
Length of the tractor-semitrailer combination, L_{TS} [m]	20.51
Width of the tractor-semitrailer combination, W_T, W_S [m]	2.55
Front overhang, f_{oh_t}	1.50
Rear overhang, r_{oh_s}	2.80
Mass parameters of the tractor/semitrailer unit	
Tractor sprung mass, $m_{sm,t}$ [kg]	8739
Tractor front axle mass, m_{fa} [kg]	746
Tractor rear axle mass, m_{ra} [kg]	1355
Tractor sprung mass moment of inertia about its x-axis, $J_{t,x}$ [kgm^2]	15000
Tractor front axle moment of inertia about its x-axis, $J_{fa,x}$ [kgm^2]	315
Tractor rear axle moment of inertia about its x-axis, $J_{ra,x}$ [kgm^2]	657
Tractor moment of inertia about its z-axis, $J_{t,z}$ [kgm^2]	21500
Sprung mass of the empty semitrailer, $m_{sm,s}$ [kg]	8100
Equivalent semitrailer axle mass, m_{sa} [kg]	1800
Semitrailer sprung mass moment of inertia about its x-axis, $J_{s,x}$ [kgm^2]	85500
Equivalent semitrailer axle moment of inertia relative to its x_{sa}-axis, $J_{sa,x}$ [kgm^2]	750
Semitrailer moment of inertia about its z-axis, $J_{s,z}$ [kgm^2]	151000
Oscillatory parameters of the tractor/semitrailer unit	
Air spring stiffness on the tractor front axle, k_{sfl}, k_{sfr} [N/m]	175000
Single shock-absorber damping on the tractor front axle, $c_{d,fa}$ [Ns/m]	20000
Equivalent shock-absorber damping on the left/right side of the tractor front axle, $c_{dfl} = 2\ c_{d,fa}$; $c_{dfr} = 2\ c_{d,fa}$ [Ns/m]	40000
Single air spring stiffness on the tractor rear axle, $k_{s,ra}$ [N/m]	200000
Equivalent air spring stiffness on the left/right side of the tractor rear axle, $k_{srl} = 2{\cdot}k_{s,ra}$; $k_{srr} = 2{\cdot}k_{s,ra}$ [N/m]	400000
Single shock-absorber damping on the tractor rear axle, $c_{d,ra}$ [Ns/m]	22500
Equivalent shock-absorber damping on the left/right side of the tractor rear axle, $c_{drl} = 2\ c_{d,ra}$; $c_{drr} = 2\ c_{d,ra}$ [Ns/m]	45000
Single tire radial stiffness on the left/right side on tractor front axle, k_{tfl}, k_{tfr} [N/m]	1000000
Equivalent tire radial stiffness on the left/right side on tractor rear axle, k_{trl}, k_{trr} [N/m]	4000000
Single air spring stiffness on the semitrailer axle, $k_{s,sa}$ [N/m]	200000
Equivalent air spring stiffness on the left/right side of the semitrailer axle, $k_{sl} = 2{\cdot}k_{s,sa}$; $k_{sr} = 2{\cdot}k_{s,sa}$ [N/m]	400000
Single shock-absorber damping on the semitrailer axle, $c_{d,sa}$ [Ns/m]	22500
Equivalent shock-absorber damping on the left/right side of the semitrailer axle, $c_{dl} = 2\ c_{d,sa}$; $c_{dr} = 2\ c_{d,sa}$ [Ns/m]	45000
Single tire radial stiffness on the left/right side on semitrailer axle, k_{tfl}, k_{tfr} [N/m]	1000000
Equivalent tire radial stiffness on the left/right side on semitrailer axle, k_{tsl}, k_{tsr} [N/m]	6000000
Anti-roll bar torsional stiffness on tractor front axle, $k_{arb,fa}$ [Nm/rad]	120000
Anti-roll bar torsional stiffness on tractor rear axle, $k_{arb,ra}$ [Nm/rad]	120000
Anti-roll bar torsional stiffness on semitrailer axle, $k_{arb,sa}$ [Nm/rad]	120000

Table 2
SUV parameters

Geometric parameters	
Wheelbase, L [m]	2.786
Distance from the front axle to the CoG, l_f [m]	1.043
Distance from the rear axle to the CoG, l_r [m]	1.743
Distance from the front right/left wheel to the roll-centre at the front RC_f, b_f [m]	0.776
Distance from the rear right/left wheel to the roll-centre at the rear RC_r, b_r [m]	0.776
Distance from the CoG of the whole vehicle to the ground, $h_{CoG,\ stat.}$ [m]	0.605
Height of the roll-centre at the front, $h_{RCfa,\ stat.}$ [m]	0.250
Height of the roll-centre at the rear, $h_{RCra,\ stat.}$ [m]	0.100
Distance from the CoG to the roll-centre at the front, $h_{RCfa,\ stat.}$ [m]	0.355
Distance from the CoG to the roll-centre at the rear, $h_{RCra,\ stat.}$ [m]	0.505
Length, L_{SUV} [m]	4.619
Width, W_{SUV} [m]	1.828
Front overhang, f_{oh_suv} [m]	0.733
Rear overhang, r_{oh_suv} [m]	1.10
Mass parameters	
Sprung mass, m_s [kg]	1900
Unsprung mass, m_t [kg]	50
Sprung mass moment of inertia about its x-axis, J_{sx} [kgm^2]	350
Moment of inertia about z-axis J_z [kgm^2]	2100
Oscillatory parameters	
Spring stiffness on the left/right side at the front, k_{sfl}, k_{sfr} [N/m]	25000
Shock-absorber damping on the left/right side at the front, c_{sfl}, c_{sfr} [Ns/m]	3250
Spring stiffness on the left/right side at the rear, k_{srl}, k_{srr} [N/m]	25000
Shock-absorber damping on the left/right side at the rear, c_{srl}, c_{srr} [Ns/m]	3250
Tire radial stiffness on the left/right side at the front, k_{tfl}, k_{tfr} [N/m]	250000
Tire radial stiffness on the left/right side at the rear, k_{trl}, k_{trr} [N/m]	250000
Tire damping on the left/right side at the front, c_{tfl}, c_{tfr} [Ns/m]	150
Tire damping on the left/right side at the rear, c_{trl}, c_{trr} [Ns/m]	150
Anti-roll bar torsional stiffness at the front, $k_{arb,f}$ [Nm/rad]	14000
Anti-roll bar torsional stiffness at the rear, $k_{arb,r}$ [Nm/rad]	14000

Table 3
Other notations

$O_1x_1y_1z_1$; $O_2x_2y_2z_2$; $O_3x_3y_3z_3$	Vehicle coordinate systems
δ	Steering angle for the vehicle front left/right wheel [rad]
F_{yfa}; F_{yra}; F_{ysa}	Tire lateral forces at the tractor front/rear axle, semitrailer axle [N]
F_{yfl}; F_{yfr}; F_{yrl}; F_{yrr}	Tire lateral forces at the SUV front left/right wheel, rear left/right wheel [N]
$F_{arb,\ rl}$; $F_{yarb,\ rr}$	Anti-roll bar force on the rear left/right SUV wheel [N]
φ_{xs}, ω_{xs}, $\dot{\omega_{xs}}$	Roll-angle motion/rate/acceleration of the SUV body [rad; rad/s; rad/s^2]
z, $\dot{z}$, $\ddot{z}$	Vertical motion/velocity/acceleration of the SUV body [m; m/s; m/s^2]
$z_{B'}$, $\dot{z}_{B'}$, $\ddot{z}_{B'}$	Vertical motion/velocity/acceleration of the SUV front left wheel [m; m/s; m/s^2]
$z_{A'}$, $\dot{z}_{A'}$, $\ddot{z}_{A'}$	Vertical motion/velocity/acceleration of the SUV front right wheel [m; m/s; m/s^2]
$z_{D'}$, $\dot{z}_{D'}$, $\ddot{z}_{D'}$	Vertical motion/velocity/acceleration of the SUV rear left wheel [m; m/s; m/s^2]
$z_{C'}$, $\dot{z}_{C'}$, $\ddot{z}_{C'}$	Vertical motion/velocity/acceleration of the SUV rear right wheel [m; m/s; m/s^2]
v_x, $\dot{v_y}$	Longitudinal velocity, lateral acceleration of the SUV CoG in vehicle fixed coordinate system [m/s; m/s^2]
a_y	Total lateral acceleration of the SUV CoG in vehicle fixed coordinate system [m/s^2]
Ψ, ω_z, $\dot{\omega_z}$	SUV yaw motion/rate/acceleration [rad; rad/s; rad/s^2]
φ_1, $\dot{\varphi_1}$	Roll-angle motion/rate for the tractor sprung mass [rad; rad/s]
ζ_{tfr}, ζ_{tfl}	Vertical excitations of the front right/left wheel
ζ_{trr}, ζ_{trl}	Vertical excitations of the rear right/left wheel
ζ_{fa}, ζ_{ra}	Road roughness below the tractor front/rear axle CoGs
ζ_{sa}	Road roughness below the semitrailer axle CoG
ζ_1, ζ_2	Road roughness below the rotational centre of the tractor/semitrailer sprung mass (RC_t, RC_s)
μ	Road friction coefficient (dry/wet asphalt) 0.7 [-]
g	Gravitational acceleration 9.81 [m/s^2]
$v_{y\ br,fa}$, $v_{y\ br,ra}$	Lateral velocity of the bridge deck at the tire contact point for the SUV front/rear wheels [m/s]
C_{cy}	Cornering stiffness coefficient (for the TS tire 7; for the SUV tire 12.5) [(N/rad)/N]
l_{s3}	Distance between the semitrailer first and second axle (Figs. 13), 1.3 [m]
Δh_{sm}	Vertical distance from the SUV CoG to the vehicle roll-axis (point *RC*)
Δh_{sf}, Δh_{sr}	Vertical distance from the SUV CoG of the sprung mass to the front/rear roll-centres
A	Tractor frontal area 10 [m^2]
A_{SUV}	SUV frontal area 2.46 [m^2]
ρ	Air density 1.29 [kg/m^3]

References

Bhat, et al., 2020. Driver Influence on Vehicle Track-Ability on Floating Bridges. TME180 Automotive Engineering Project. Chalmers University of Technology, Gothenburg, Sweden. https://odr.chalmers.se/handle/20.500.12380/300748.

Brandt, A., Jacobson, B., Sebben, S., 2021. High speed driving stability of road vehicles under crosswinds: an aerodynamic and vehicle dynamic parametric sensitivity analysis. Veh. Syst. Dyn. https://doi.org/10.1080/00423114.2021.1903516.

Chen, S.R., Cai, C.S., 2004. Accident assessment of vehicles on long-span bridges in windy environments. J. Wind Eng. Ind. Aerod. 92 (12), 991–1024.

Dineff, et al., 2021. Aerodynamic Investigations of a Simplified Truck under High Yaw Wind Conditions. Chalmers University of Technology, Gothenburg, Sweden (2021). *https://odr.chalmers.se/handle/20.500.12380/302252*.

Ghandriz, T., Jacobson, B., Nilsson, P., Laine, L., Fröjd, N., 2020. Computationally efficient nonlinear one- and two-track models for multitrailer road vehicles. IEEE Access 8, 203854–203875.

Gillespie, T., 1992. Fundamentals of Vehicle Dynamics. SAE, Warrendale PA, USA.

Guo, W.H., Xu, Y.L., 2006. Safety analysis of moving road vehicles on a long bridge under crosswind. J. Eng. Mech. 132 (4), 438–446.

Gustafsson, A., et al., 2019. Driver Influence on Vehicle Track-Ability on Floating Bridges. Bachelor's Thesis in Mechanical Engineering. Department of Mechanics and Maritime Sciences, Chalmers University of Technology, Gothenburg, Sweden. https://odr.chalmers.se/handle/20.500.12380/256914.

ISO, 1995 8608 ISO, 1995. Mechanical Vibration-Road Surface Profiles-Reporting of Measured Data International Standards Organization, Switzerland.

Jacobson, et al., 2020. Vehicle Dynamics Compendium. Chalmers University of Technology. https://research.chalmers.se/publication/513850/file/513850_Fulltext.pdf.

Jeyed, A.H., Ali Ghaffari, A., 2019. Development of a novel nonlinear estimator based on state-dependent Riccati equation technique for articulated vehicles. Proc IMechE Part K: J Multi-body Dynamics 233 (3), 516–530.

Lin, R.C., Cebon, D., Cole, D.J., 1996. Active roll control of articulated vehicles. Veh. Syst. Dyn. 26 (1), 17–43.

Liu, P.J., Rakheja, S., Ahmed, A.K.W., 2001. Dynamic roll instability analysis of heavy vehicles using energy approach. Int. J. Heavy Veh. Syst. 8 (2), 177–195.

Nguyen, V.M., Le, V.Q., 2019. Ride comfort performance of heavy truck with three control cases of semi-active isolation systems. Vibroengineering PROCEDIA 22, 93–98.

Nguyen, K., Camara, A., Rio, O., Sparowitz, L., 2017. Dynamic effects of turbulent crosswind on the serviceability state of vibrations of a slender arch bridge including wind–vehicle–bridge interaction. J. Bridge Eng. 22 (11), 06017005.

Pacejka, H.B., 2012. Tire and Vehicle Dynamics, third ed. Elsevier/BH, Amsterdam.

Sekulic, D., 2018. Effect of Floating Bridge Vertical Motion on Vehicle Ride Comfort and Road Grip. https://www.vegvesen.no/_attachment/2487039/binary/1294853?fast_title=Effect+of+floating+bridge+vertical+motion+on+vehicle+ride+comfort+and+road+grip.pdf.

Sekulic, D., et al., 2013. Analysis of vibration effects on the comfort of intercity bus users by oscillatory model with ten degrees of freedom. Appl. Math. Model. 37 (18), 8629–8644.

Sekulic, D., Jacobson, B., Moe, S.J., Svangstu, E., 2020a. Effect of floating bridge motion on vehicle ride comfort and road grip. In: The IAVSD International Symposium on Dynamics of Vehicles on Roads and Tracks. Springer, Cham, pp. 1416–1424.

Sekulic, D., Vdovin, A., Jacobson, B., Sebben, S., Johannesen, M.S., 2020b. Effects of wind loads and floating bridge motion on intercity bus lateral stability. J. Wind Eng. Ind. Aerod. 212, 1–18, 104589.

Shyrokau, B., Wang, D., Savitski, D., Ivanov, D., 2013. Vehicle dynamics control with energy recuperation based on control allocation for independent wheel motors and brake system. Int. J. Powertrains 2 (2/3), 153–181.

Siringoringo, D.M., Fujino, Y., 2012. Estimating bridge fundamental frequency from vibration response of instrumented passing vehicle: analytical and experimental study. Adv. Struct. Eng. 15 (3), 417–434.

Software, M.S.C., 2013. Adams/Car Truck Help – Adams, USA.

Vegvesen, 2015. N400 Bruprosjektering. Prosjektering Av Bruer, Ferjekaier Og Andre.

Vegvesen, 2017. SBJ-31-C3-MUL-22-RE-100 - Analysis and Design (Base Case) Bjørnafjorden, Straight Floating Bridge Phase 3 Analysis and Design (Base Case).

Vegvesen, 2021. https://www.vegvesen.no/globalassets/vegprosjekter/utbygging/ferjefrie39/vedlegg/faktaark/lonnsomhet-for-godstransport.pdf.

Wang, W., Hariharan, S.V., 2021. Aerodynamic Investigations of Vehicles under High Side Wind Conditions on Bridges. Master Thesis. Department of Mechanics and Maritime Sciences, Chalmers University of Technology, Gothenburg, Sweden. https://hdl.handle.net/20.500.12380/303654.

Yang, X., Song, J., Gao, J., 2015. Fuzzy logic based control of the lateral stability of tractor semitrailer vehicle. Math. Probl Eng. 2015. Article ID 692912, 16 pp.

Zhang, C., et al., 2019. Introduction of the AeroSUV-A New Generic SUV Model for Aerodynamic Research. https://doi.org/10.4271/2019-01-0646. SAE Technical Paper.

Zhu, J., Zhang, W., Wu, M.X., 2018. Evaluation of ride comfort and driving safety for moving vehicles on slender coastal bridges. J. Vib. Acoust. 140 (5), 051012.